Supporting Information

Engineered Multivariate Metal-Organic Frameworks for Magnetic Resonance Molecular Imaging Signal Enhancement

Zhen Wang[†‡§], Qingbin Zeng[†‡§], Chenlu Yuan[†‡], Xinxin Yang[†‡], Wei Song[†‡], Yaping Yuan[†‡], Xiuchao Zhao[†‡], Daiqin Chen[†‡], Yuqi Yang[†‡], Qianni Guo[†‡], Xin Zhou[†‡¶*]*

[†] State Key Laboratory of Magnetic Resonance Spectroscopy and Imaging, National Center for Magnetic Resonance in Wuhan, Wuhan Institute of Physics and Mathematics, Innovation Academy for Precision Measurement Science and Technology, Chinese Academy of Sciences, Wuhan 430071, P. R. China.

[‡] University of Chinese Academy of Sciences, Beijing 100049, P. R. China.

[¶] School of Biomedical Engineering, Hainan University, Haikou 570228, P. R. China.

[*] Email: qian-niguo@wipm.ac.cn, xinzhou@wipm.ac.cn

[§] Z.W. and Q.Z. contributed equally to this work.

1 Preparation of CAU-1

1.1 Materials and instruments

Aluminum chloride hexahydrate ($AlCl_3 \cdot 6H_2O$), anhydrous methanol, anhydrous ethanol, N, N-dimethylformamide (DMF) were purchased from Sinopharm Chemical Reagent Co. Ltd (China). 2-aminoterephthalic (NH_2-BDC) acid and 2-hydroxyterephthalic acid (OH-BDC), 2-methoxyterephthalic acid (MeO-BDC) were purchased from Aladdin (Shanghai). All chemicals were commercially obtained and used without further purification.

The synthesized nanoparticles were characterized by transmission electron microscopy (TEM, JEM-2100), field emission scanning electron microscope (SEM, ZEISS Gemini SEM 500), powder X-ray Diffraction (PXRD), X-ray photoelectron spectroscopy (XPS, Thermo Scientific K-Alpha), N_2 adsorption analysis (BELSORP-max), Fourier Transform infrared spectroscopy (FTIR, Thermo Scientific Nicolet iS10), Thermal gravimetric analysis (TGA, TGA Q500). Hyperpolarized ^{129}Xe NMR and ^{129}Xe MRI experiments were carried out using a 400 MHz Bruker AV400 wide-bore spectrometer (Bruker Biospin, Ettlingen, Germany). Solid-state ^{1}H MAS NMR were carried out using a Bruker Avance III 400 MHz solid-state NMR spectrometer (Bruker Biospin, Ettlingen, Germany).

1.2 Synthesis procedures

CAU-1-OH

- Low-crystallinity phase: 71.9 mg OH-BDC (0.05 M) and 286.1 mg $AlCl_3 \cdot 6H_2O$ (0.15 M) were dissolved in 7.9 mL MeOH under ultrasonication.
- 230 nm: 100.7 mg OH-BDC (0.07 M) and 400.5 mg $AlCl_3 \cdot 6H_2O$ (0.21 M) were dissolved in 7.9 mL MeOH under ultrasonication.
- 550 nm: 172.6 mg OH-BDC (0.12 M) and 686.6 mg $AlCl_3 \cdot 6H_2O$ (0.36 M) were dissolved in 7.9 mL MeOH under ultrasonication.
- 800 nm: 215.7 mg OH-BDC (0.15 M) and 858.3 mg $AlCl_3 \cdot 6H_2O$ (0.45 M) were dissolved in 7.9 mL MeOH under ultrasonication.

CAU-1-NH_2

- Low-crystallinity phase: 71.6 mg NH_2-BDC (0.05 M) and 286.1 mg $AlCl_3 \cdot 6H_2O$ (0.15 M) were dissolved in 7.9 mL MeOH under ultrasonication.
- 210 nm: 100.2 mg NH_2-BDC (0.07 M) and 400.5 mg $AlCl_3 \cdot 6H_2O$ (0.21 M) were dissolved in 7.9 mL MeOH under ultrasonication.

- 300 nm: 143.2 mg NH_2-BDC (0.10 M) and 572.2 mg $AlCl_3 \cdot 6H_2O$ (0.30 M) were dissolved in 7.9 mL MeOH under ultrasonication.
- 900 nm: 243.4 mg NH_2-BDC (0.17 M) and 858.3 mg $AlCl_3 \cdot 6H_2O$ (0.51 M) were dissolved in 7.9 mL MeOH under ultrasonication.

CAU-1-$(OH)_x$-$(NH_2)_{1-x}$
CAU-1-$(OH)_{0.5}$-$(NH_2)_{0.5}$:
- 35 nm: 36.0 mg OH-BDC (0.025 M), 35.8 mg NH_2-BDC (0.025 M) and 286.1 mg $AlCl_3 \cdot 6H_2O$ (0.15 M) were dissolved in 7.9 mL MeOH under ultrasonication.
- 200 nm: 50.4 mg OH-BDC (0.035 M), 50.1 mg NH_2-BDC (0.035 M) and 400.5 mg $AlCl_3 \cdot 6H_2O$ (0.21 M) were dissolved in 7.9 mL MeOH under ultrasonication.
- 650 nm: 86.3 mg OH-BDC (0.06 M), 85.8 mg NH_2-BDC (0.06 M) and 686.6 mg $AlCl_3 \cdot 6H_2O$ (0.36 M) were dissolved in 7.9 mL MeOH under ultrasonication.
- 900 nm: 107.9 mg OH-BDC (0.075 M), 107.3 mg NH_2-BDC (0.075 M) and 858.3 mg $AlCl_3 \cdot 6H_2O$ (0.45 M) were dissolved in 7.9 mL MeOH under ultrasonication.

Different ligand ratios:
- CAU-1-$(OH)_{0.9}$-$(NH_2)_{0.1}$: 90.6 mg OH-BDC (0.063 M), 10.0 mg NH_2-BDC (0.007 M) and 400.5 mg $AlCl_3 \cdot 6H_2O$ (0.21 M) were dissolved in 7.9 mL MeOH under ultrasonication.
- CAU-1-$(OH)_{0.8}$-$(NH_2)_{0.2}$: 80.6 mg OH-BDC (0.056 M), 20.0 mg NH_2-BDC (0.014 M) and 400.5 mg $AlCl_3 \cdot 6H_2O$ (0.21 M) were dissolved in 7.9 mL MeOH under ultrasonication.
- CAU-1-$(OH)_{0.7}$-$(NH_2)_{0.3}$: 70.5 mg OH-BDC (0.049 M), 30.1 mg NH_2-BDC (0.021 M) and 400.5 mg $AlCl_3 \cdot 6H_2O$ (0.21 M) were dissolved in 7.9 mL MeOH under ultrasonication.
- CAU-1-$(OH)_{0.6}$-$(NH_2)_{0.4}$: 60.4 mg OH-BDC (0.042 M), 40.1 mg NH_2-BDC (0.028 M) and 400.5 mg $AlCl_3 \cdot 6H_2O$ (0.21 M) were dissolved in 7.9 mL MeOH under ultrasonication.
- CAU-1-$(OH)_{0.4}$-$(NH_2)_{0.6}$: 40.3 mg OH-BDC (0.028 M), 60.1 mg NH_2-BDC (0.042 M) and 400.5 mg $AlCl_3 \cdot 6H_2O$ (0.21 M) were dissolved in 7.9 mL MeOH under ultrasonication.
- CAU-1-$(OH)_{0.3}$-$(NH_2)_{0.7}$: 30.2 mg OH-BDC (0.021 M), 70.1 mg NH_2-BDC (0.049 M) and 400.5 mg $AlCl_3 \cdot 6H_2O$ (0.21 M) were dissolved in 7.9 mL MeOH under ultrasonication.
- CAU-1-$(OH)_{0.2}$-$(NH_2)_{0.8}$: 20.1 mg OH-BDC (0.014 M), 80.2 mg NH_2-BDC (0.056 M) and 400.5 mg $AlCl_3 \cdot 6H_2O$ (0.21 M) were dissolved in 7.9 mL MeOH under ultrasonication.
- CAU-1-$(OH)_{0.1}$-$(NH_2)_{0.9}$: 10.1 mg OH-BDC (0.007 M), 90.2 mg NH_2-BDC (0.063 M) and 400.5 mg $AlCl_3 \cdot 6H_2O$ (0.21 M) were dissolved in 7.9 mL MeOH under ultrasonication.

CAU-1-$(OMe)_{0.5}$-$(NH_2)_{0.5}$:

- 54.0 mg MeO-BDC (0.035 M), 50.1 mg NH_2-BDC (0.035 M) and 400.5 mg $AlCl_3 \cdot 6H_2O$ (0.21 M) were dissolved in 7.9 mL MeOH under ultrasonication.

  The resulting mixture was transferred to a Teflon-lined stainless-steel autoclave (15 mL) and heated at 125 °C for 5.5 h. After gently cooling down to room temperature, the solution was centrifuged at 10000 rpm for 5 min, and the bottom solid was further washed with DMF and methanol twice each, respectively. Finally, the resulting solid was heated in a vacuum drying oven at 50 °C for 24 h.

2 High performance liquid chromatography (HPLC)

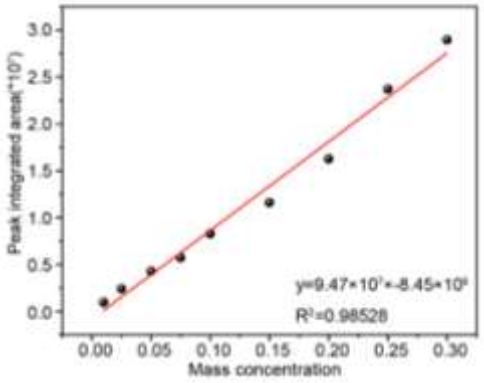

Figure S1. Standard curve of OH-BDC obtained by HPLC test.

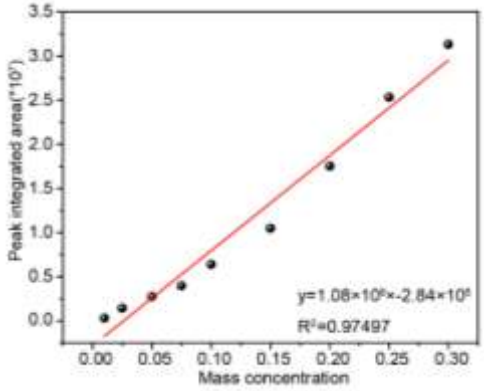

Figure S2. Standard curve of NH_2-BDC obtained by HPLC test.

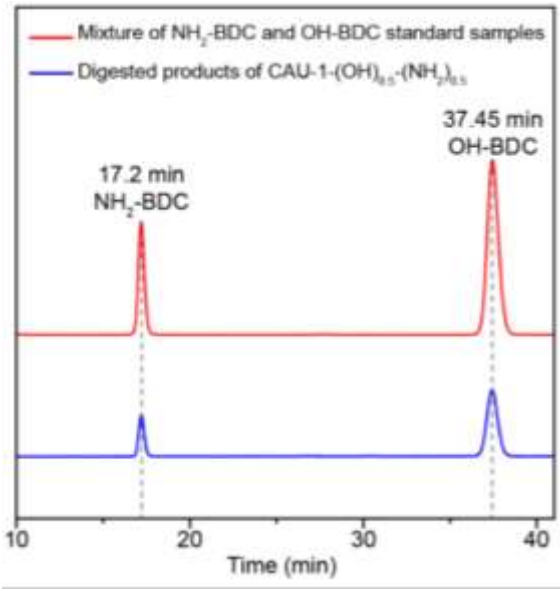

Figure S3. HPLC analysis for lysates of CAU-1-$(OH)_{0.5}$-$(NH_2)_{0.5}$ and organic ligand mixture.

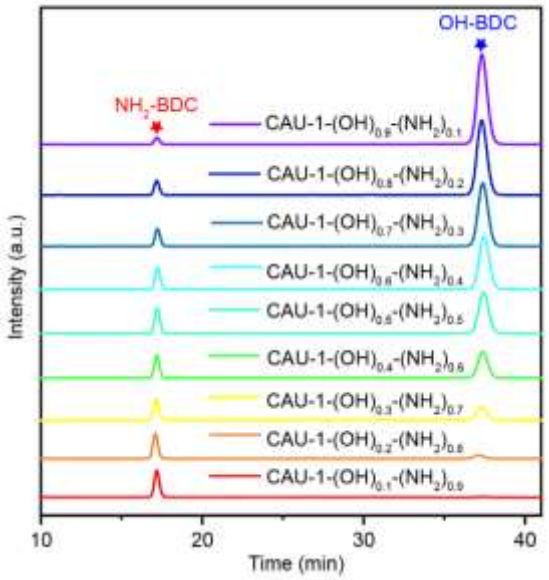

Figure S4. HPLC of lysates of MOF with different ligand ratios.

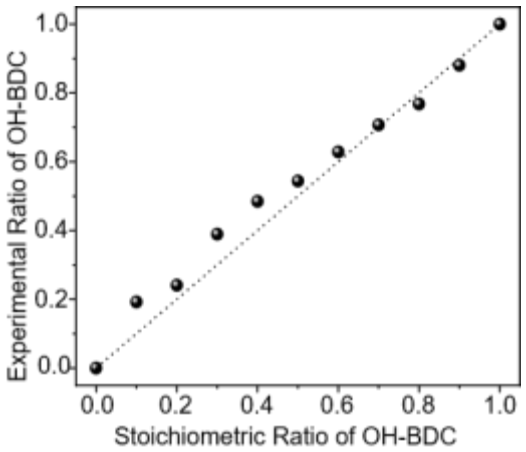

Figure S5. The trend of the proportion of OH-BDC in CAU-1-$(OH)_x$-$(NH_2)_{1-x}$ varying with the feed ratio.

3 Morphology characterization

3.1 Transmission electron microscopy (TEM)

Different particle size

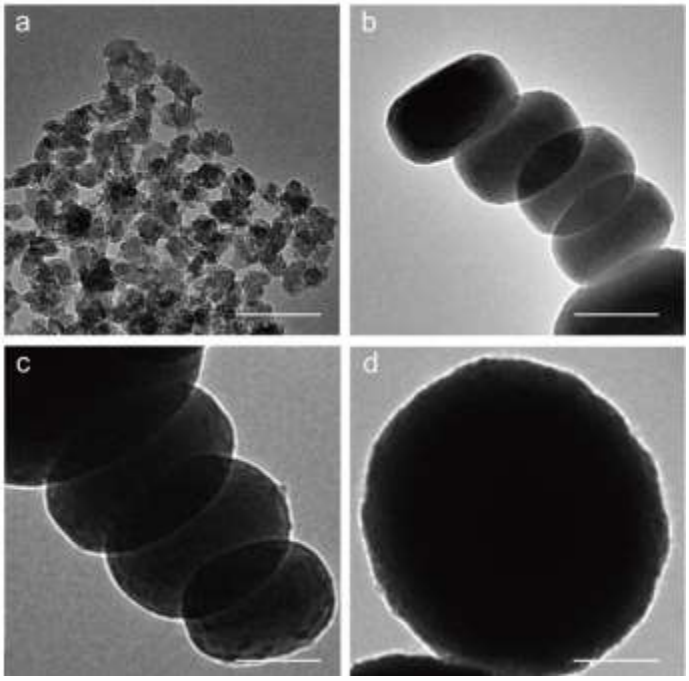

Figure S6. TEM images of CAU-1-OH nanoparticles in low-crystallinity phase (a), 230 nm (b), 550 nm (c), 800 nm (d). (Scale bar = 200 nm)

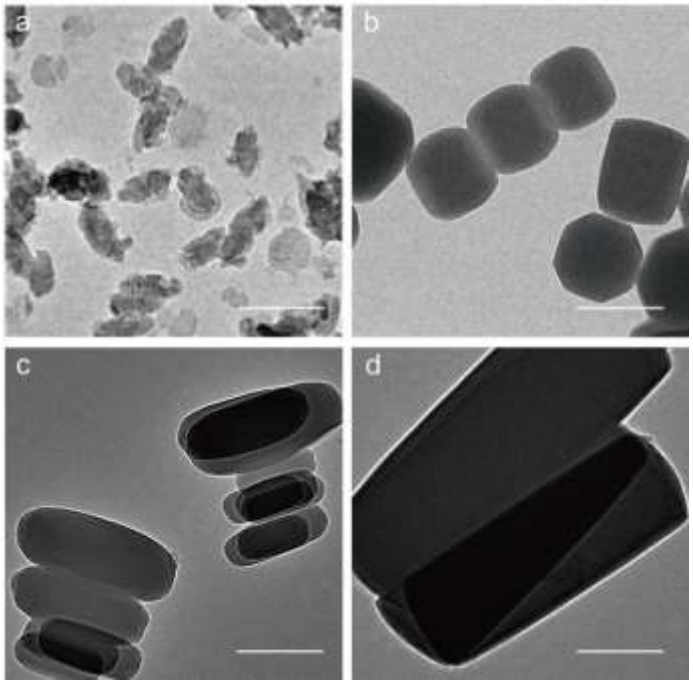

Figure S7. TEM images of CAU-1-NH_2 nanoparticles in low-crystallinity phase (a), 210 nm (b), 300 nm (c), 900 nm (d). (Scale bar = 200 nm)

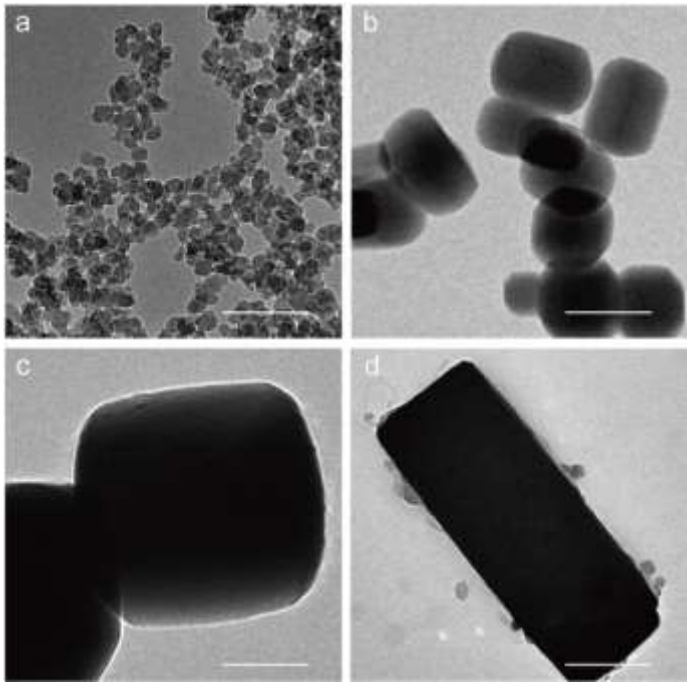

Figure S8. TEM images of CAU-1-$(OH)_{0.5}$-$(NH_2)_{0.5}$ nanoparticles in 35 nm (a), 200 nm (b), 650 nm (c), 900 nm (d). (Scale bar = 200 nm)

Different ligand ratios:

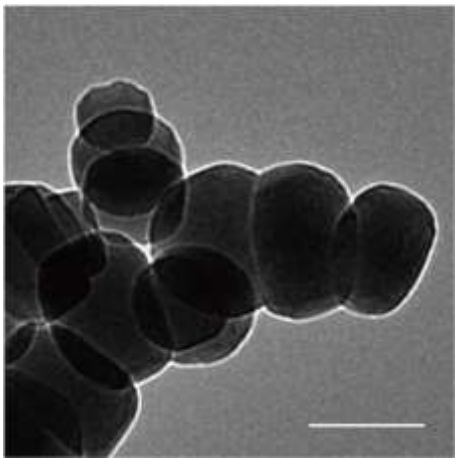

Figure S9. TEM image of CAU-1-$(OH)_{0.9}$-$(NH_2)_{0.1}$ nanoparticles. (Scale bar = 200 nm)

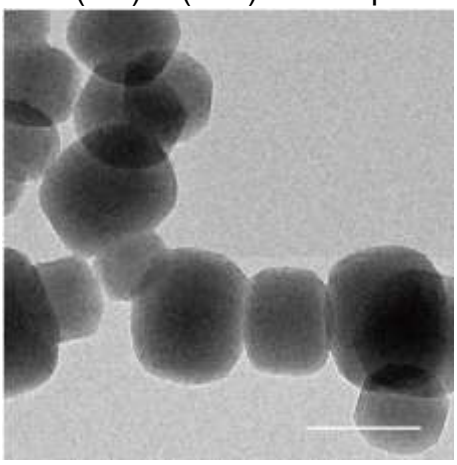

Figure S10. TEM image of CAU-1-$(OH)_{0.8}$-$(NH_2)_{0.2}$ nanoparticles. (Scale bar = 200 nm)

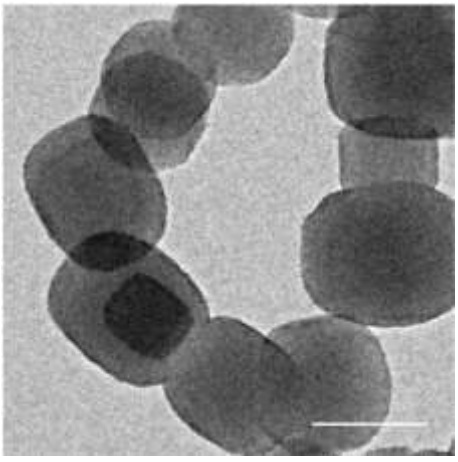

Figure S11. TEM image of CAU-1-$(OH)_{0.7}$-$(NH_2)_{0.3}$ nanoparticles. (Scale bar = 200 nm)

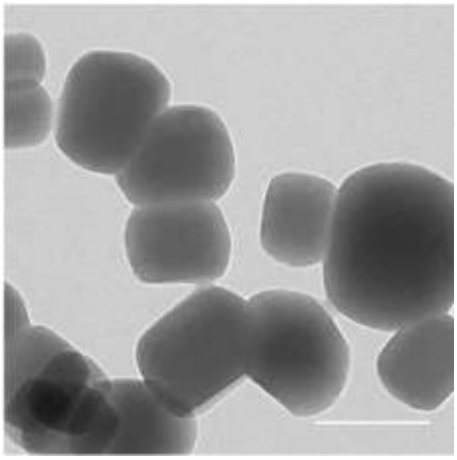

Figure S12. TEM image of CAU-1-$(OH)_{0.6}$-$(NH_2)_{0.4}$ nanoparticles. (Scale bar = 200 nm)

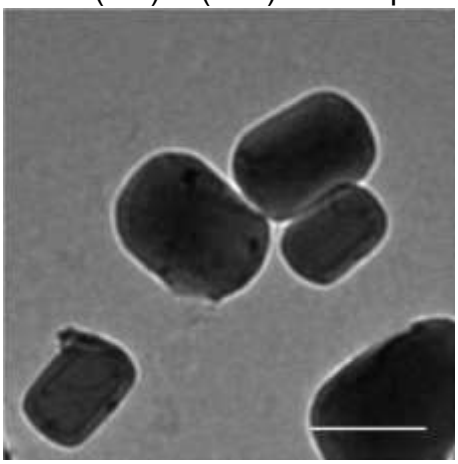

Figure S13. TEM image of CAU-1-$(OH)_{0.4}$-$(NH_2)_{0.6}$ nanoparticles. (Scale bar = 200 nm)

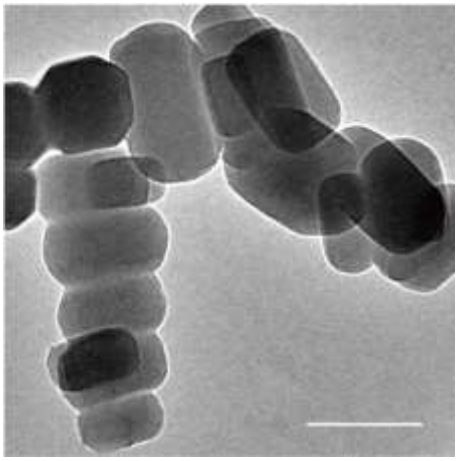

Figure S14. TEM image of CAU-1-$(OH)_{0.3}$-$(NH_2)_{0.7}$ nanoparticles. (Scale bar = 200 nm)

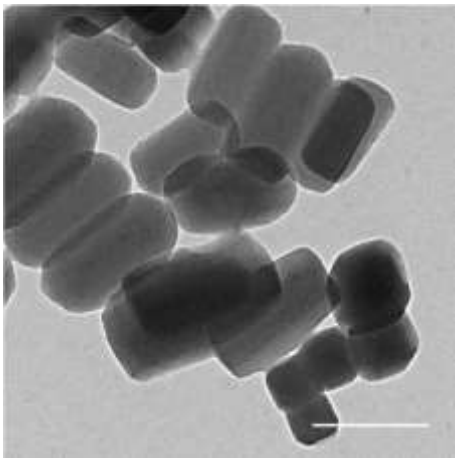

Figure S15. TEM image of CAU-1-$(OH)_{0.2}$-$(NH_2)_{0.8}$ nanoparticles. (Scale bar = 200 nm)

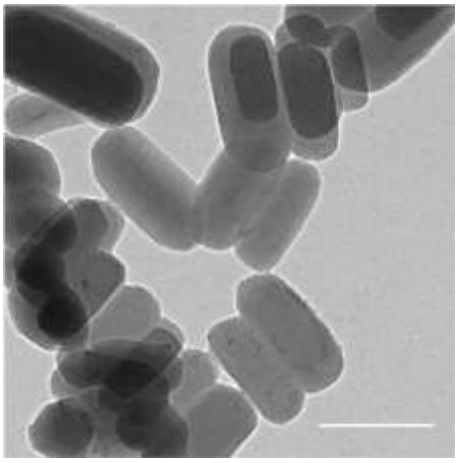

Figure S16. TEM image of CAU-1-$(OH)_{0.1}$-$(NH_2)_{0.9}$ nanoparticles. (Scale bar = 200 nm)

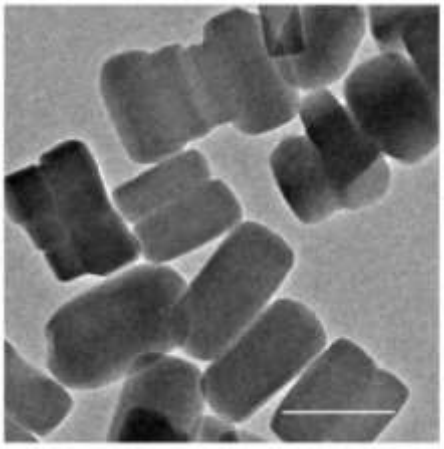

Figure S17. TEM image of CAU-1-$(OMe)_{0.5}$-$(NH_2)_{0.5}$ nanoparticles. (Scale bar = 200 nm)

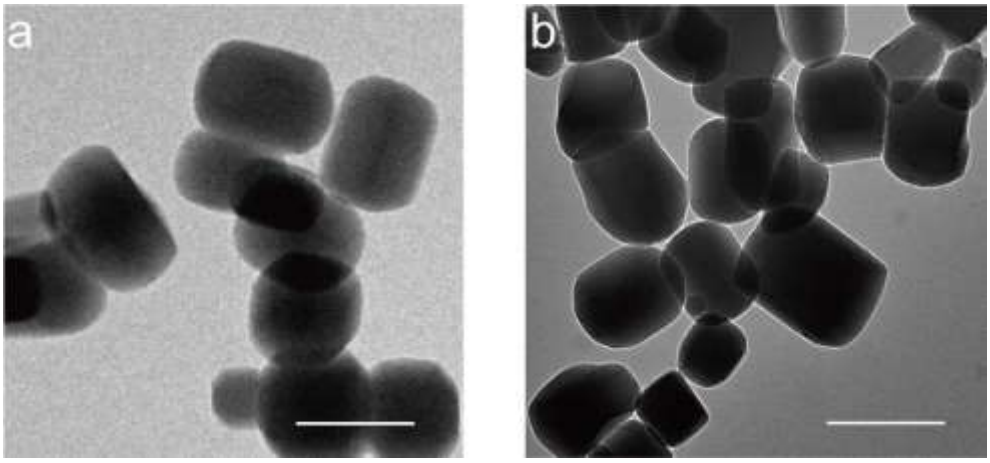

Figure S18. (a) TEM images of freshly prepared CAU-1-$(OH)_{0.5}$-$(NH_2)_{0.5}$ nanoparticles. (b) TEM image of CAU-1-$(OH)_{0.5}$-$(NH_2)_{0.5}$ soaked in water for 1 month. (Scale bar = 200 nm)

3.2 Scanning electron microscopy (SEM)

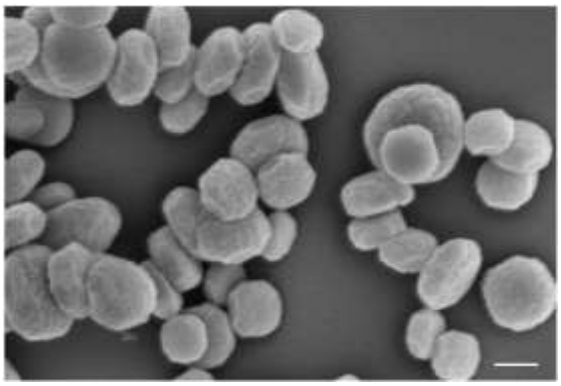

Figure S19. SEM image of CAU-1-OH nanoparticles. (Scale bar = 200 nm)

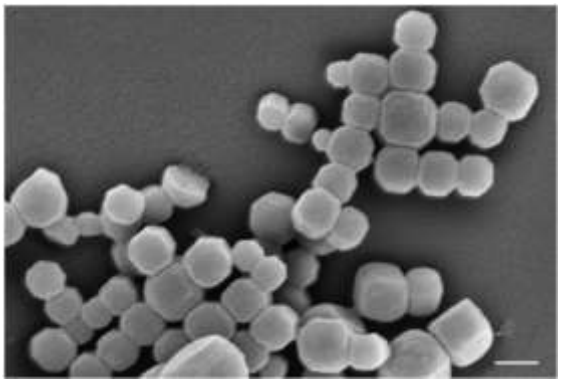

Figure S20. SEM image of CAU-1-NH_2 nanoparticles. (Scale bar = 200 nm)

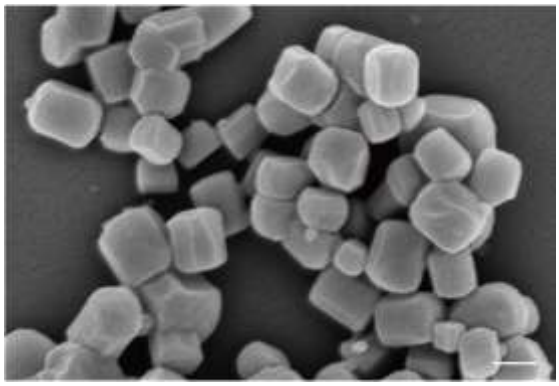

Figure S21. SEM image of CAU-1-$(OH)_{0.5}$-$(NH_2)_{0.5}$ nanoparticles. (Scale bar = 200 nm)

Different ligand ratios:

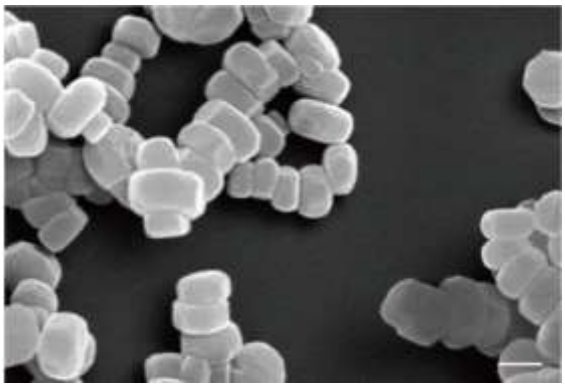

Figure S22. SEM image of CAU-1-$(OH)_{0.9}$-$(NH_2)_{0.1}$ nanoparticles. (Scale bar = 200 nm)

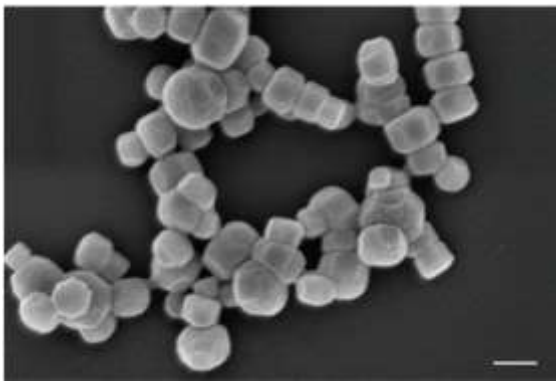

Figure S23. SEM image of CAU-1-$(OH)_{0.8}$-$(NH_2)_{0.2}$ nanoparticles. (Scale bar = 200 nm)

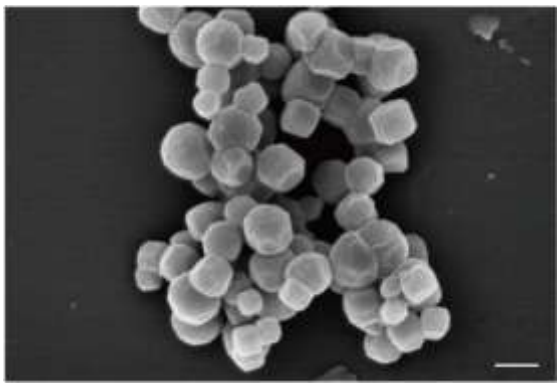

Figure S24. SEM image of CAU-1-$(OH)_{0.7}$-$(NH_2)_{0.3}$ nanoparticles. (Scale bar = 200 nm)

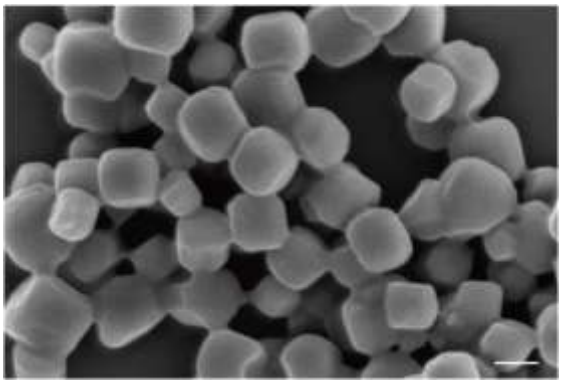

Figure S25. SEM image of CAU-1-$(OH)_{0.6}$-$(NH_2)_{0.4}$ nanoparticles. (Scale bar = 200 nm)

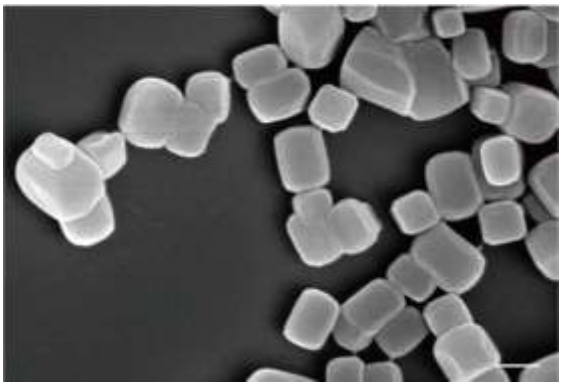

Figure S26. SEM image of CAU-1-$(OH)_{0.4}$-$(NH_2)_{0.6}$ nanoparticles. (Scale bar = 200 nm)

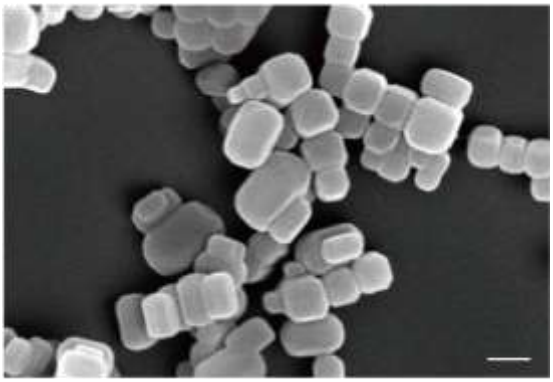

Figure S27. SEM image of CAU-1-$(OH)_{0.3}$-$(NH_2)_{0.7}$ nanoparticles. (Scale bar = 200 nm)

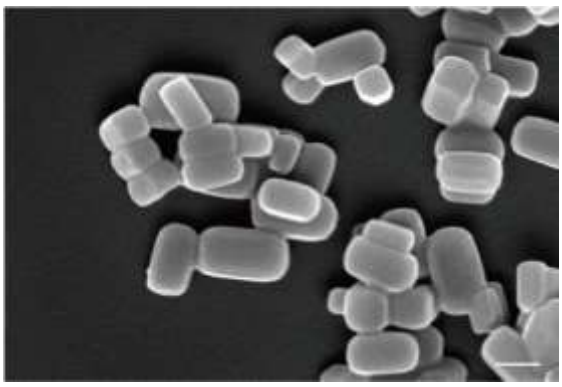

Figure S28. SEM image of CAU-1-$(OH)_{0.2}$-$(NH_2)_{0.8}$ nanoparticles. (Scale bar = 200 nm)

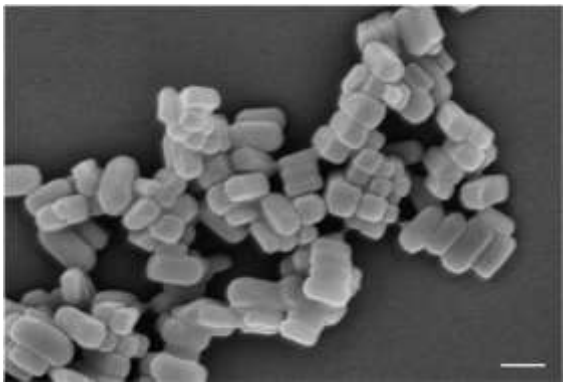

Figure S29. SEM image of CAU-1-$(OH)_{0.1}$-$(NH_2)_{0.9}$ nanoparticles. (Scale bar = 200 nm)

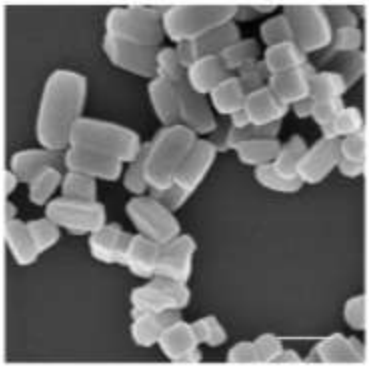

Figure S30. SEM image of CAU-1-$(OMe)_{0.5}$-$(NH_2)_{0.5}$. nanoparticles. (Scale bar = 200 nm)

3.3 EDS mapping

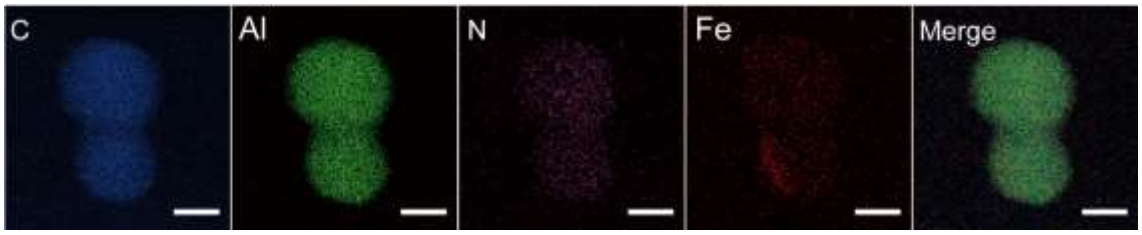

Figure S31. EDS mapping of CAU-1-$(OH)_{0.5}$-$(NH_2)_{0.5}$ reacted with Fe^{3+}.

4 X-ray Photoelectron Spectroscopy (XPS) Measurements

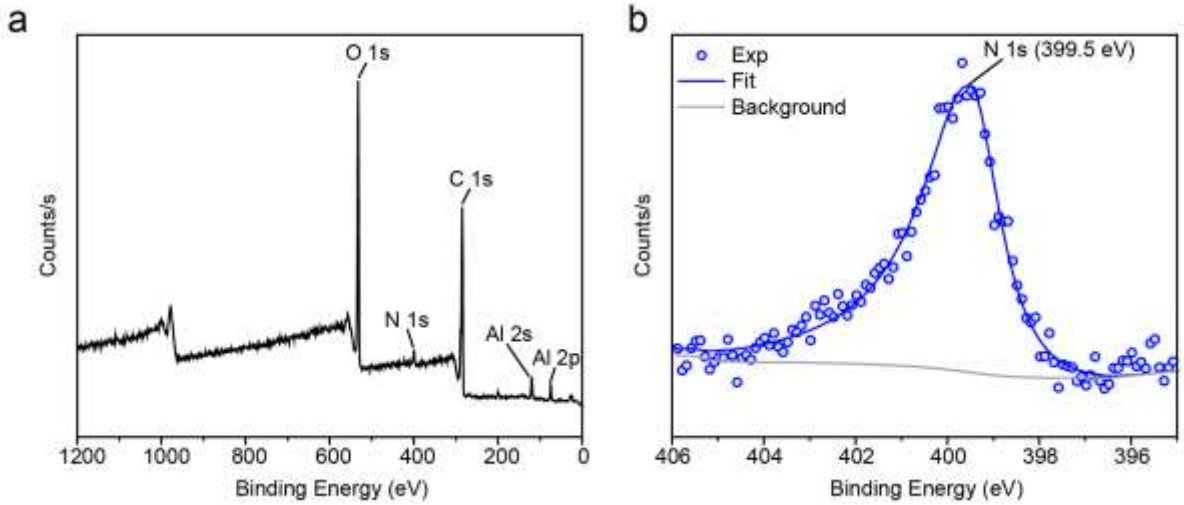

Figure S32. (a) Survey XPS spectrum of CAU-1-$(OH)_{0.5}$-$(NH_2)_{0.5}$. (b) High-resolution N 1s XPS spectrum of CAU-1-$(OH)_{0.5}$-$(NH_2)_{0.5}$.

5 Solid-state ^{1}H MAS NMR

Solid-state ^{1}H MAS NMR measurements were implemented on a Bruker Avance III 400 MHz solid-state NMR spectrometer to resolve distinct proton chemical environments of organic ligands (OH-BDC, NH_2-BDC) and two CAU-1 samples (CAU-1-NH_2, CAU-1-$(OH)_{0.5}$-$(NH_2)_{0.5}$). Prior to characterization, all powder samples were fully dried under vacuum at 60 °C overnight to remove residual adsorbed water and solvent molecules, which would generate interfering proton signals. Dried solid powders were tightly packed into 4 mm zirconia MAS rotors. ^{1}H MAS NMR spectra were recorded on a solid-state NMR spectrometer at a spinning rate of 10 kHz at room temperature.

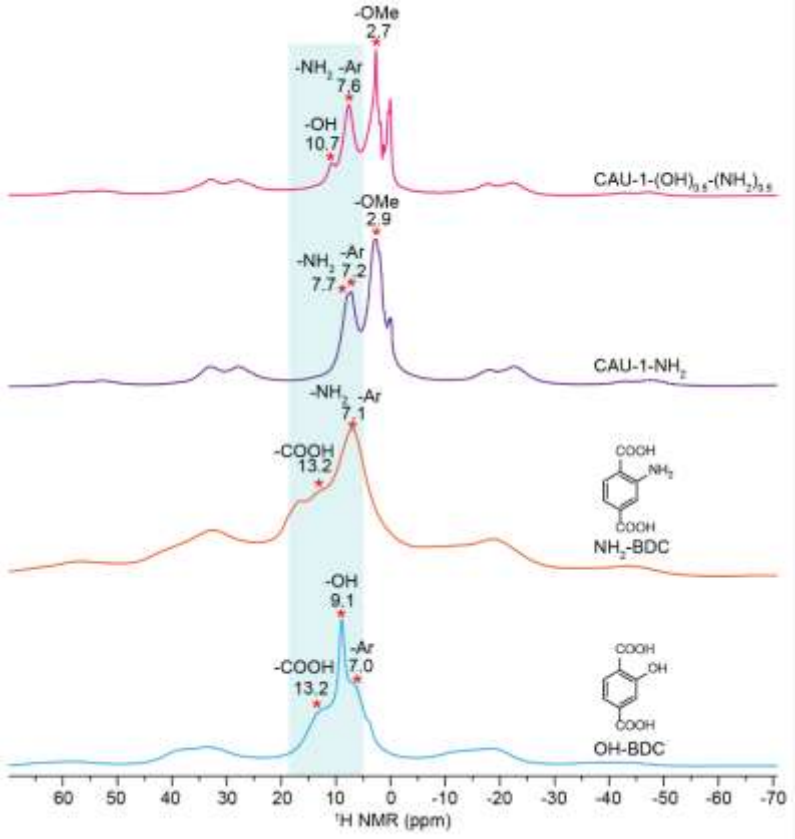

Figure S33. Solid-state ^{1}H MAS NMR spectra (10 kHz) of OH-BDC, NH_2-BDC, CAU-1-NH_2 and CAU-1-$(OH)_{0.5}$-$(NH_2)_{0.5}$. Peak assignments for different protons are marked.

6 Powder X-ray diffraction

The Powder X-ray Diffraction (PXRD) data of CAU-1 were collected on a Rigaku Smartlab diffractometer (Cu Kα).

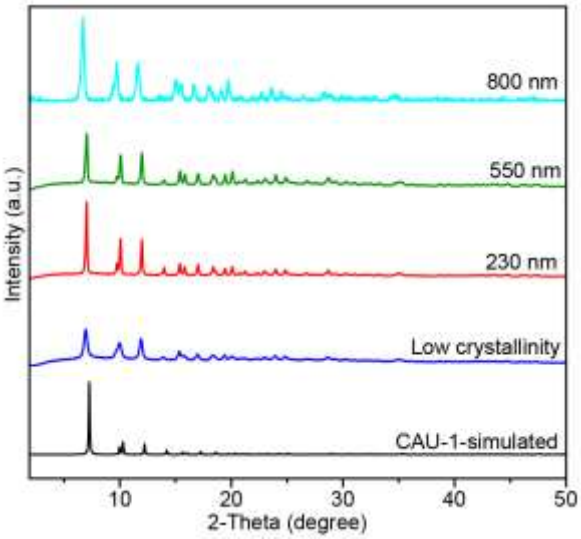

Figure S34. Comparisons of the experimental PXRD pattern of activated CAU-1-OH in different particle sizes (low crystallinity, 230, 550, and 800 nm) with the simulated diffraction pattern (black). The observed peak shift toward lower 2θ angles is attributed to lattice expansion caused by water adsorption.

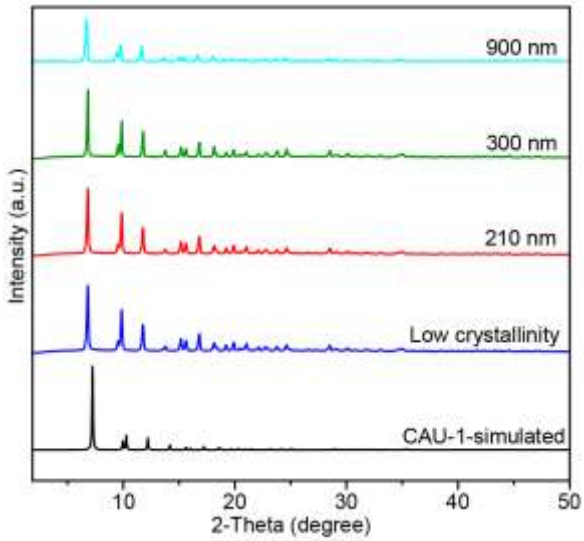

Figure S35. Comparisons of the experimental PXRD pattern of activated CAU-1-NH_2 in different particle sizes (low crystallinity, 210, 300, and 900 nm) with the simulated

diffraction pattern (black). The observed peak shift toward lower 2θ angles is attributed to lattice expansion caused by water adsorption.

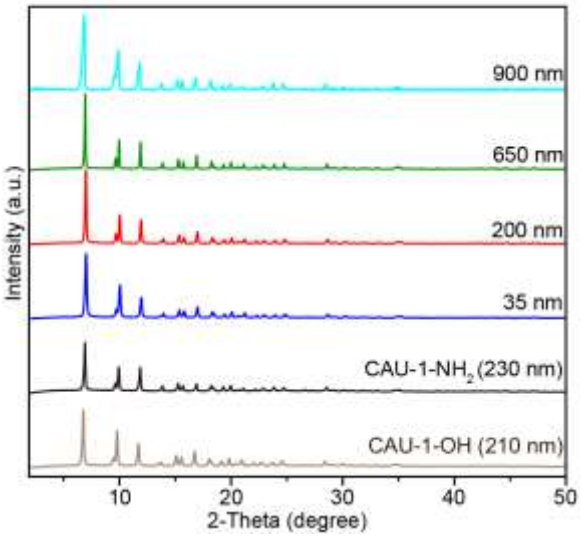

Figure S36. Comparisons of the experimental PXRD pattern of activated CAU-1-$(OH)_{0.5}$-$(NH_2)_{0.5}$ in different particle sizes (35, 200, 650, and 900 nm) with the single component CAU-1-OH and CAU-1-NH_2.

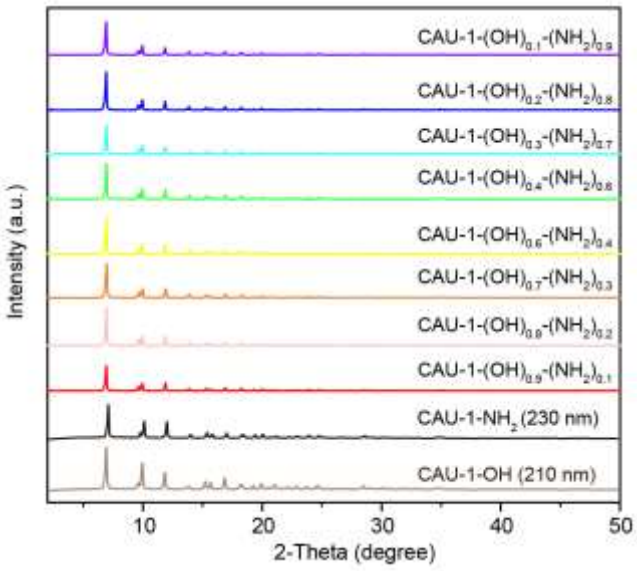

Figure S37. Comparisons of the experimental PXRD pattern of activated CAU-1-$(OH)_x$-$(NH_2)_{1-x}$ at different ligand ratios with the single component CAU-1-OH and CAU-1 NH_2.

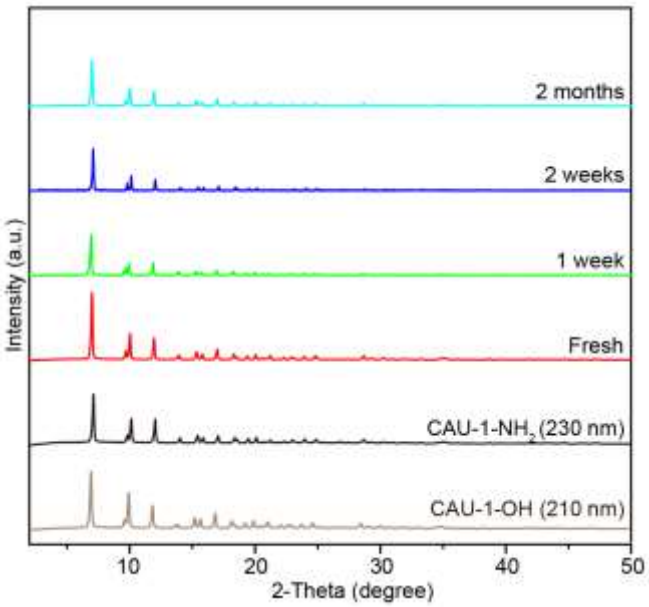

Figure S38. PXRD patterns of CAU-1-$(OH)_{0.5}$-$(NH_2)_{0.5}$ (200 nm) were collected during the stability test in water at room temperature. The framework structure of CAU-1-$(OH)_{0.5}$-$(NH_2)_{0.5}$ remained unchanged after being immersed in water for 2 months.

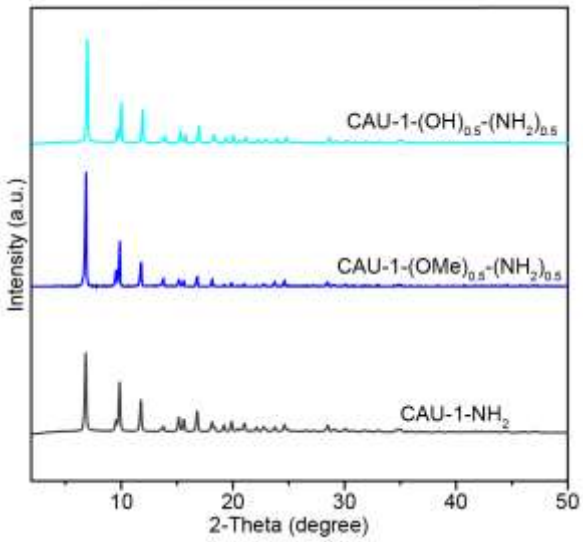

Figure S39. Comparisons of the experimental PXRD pattern of activated CAU-1-$(OMe)_{0.5}$-$(NH_2)_{0.5}$ with the CAU-1-$(OH)_{0.5}$-$(NH_2)_{0.5}$ and CAU-1-NH_2.

7 Thermogravimetric analysis (TGA)

All measurements were performed on a TGA Q500 thermal gravimetric analyzer with samples held in aluminum oxide pans in a continuous airflow atmosphere.

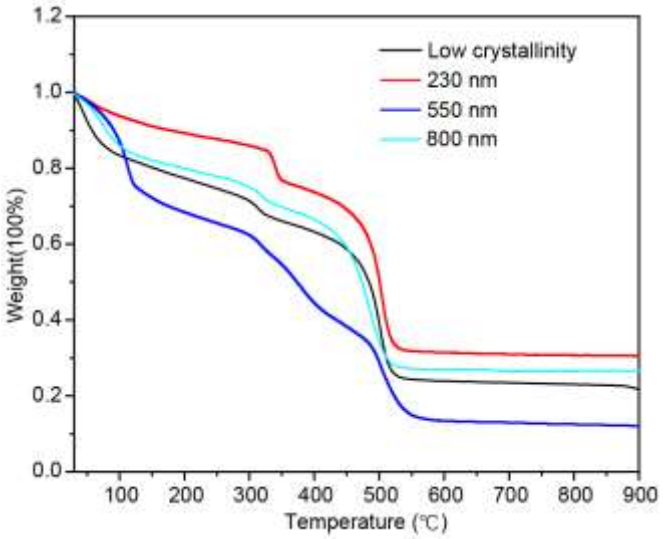

Figure S40. TGA trace of CAU-1-OH.

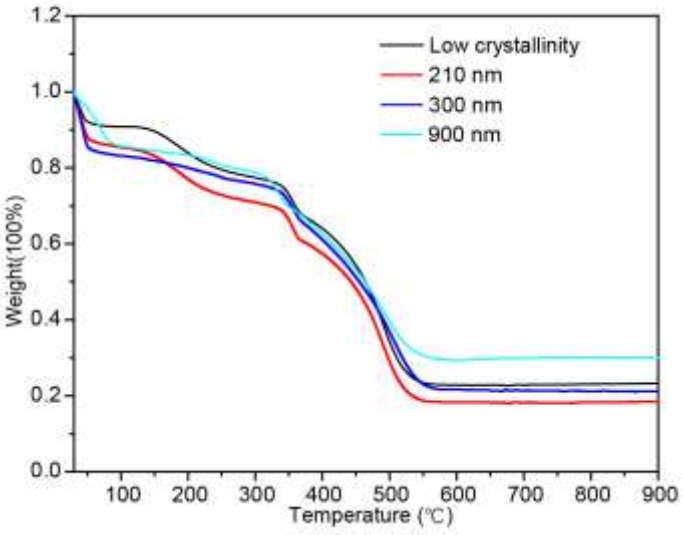

Figure S41. TGA trace of CAU-1-NH_2.

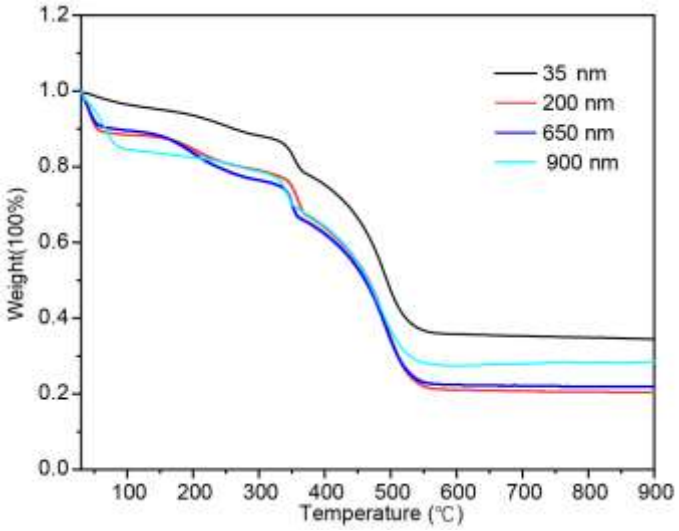

Figure S42. TGA trace of CAU-1-$(OH)_{0.5}$-$(NH_2)_{0.5}$.

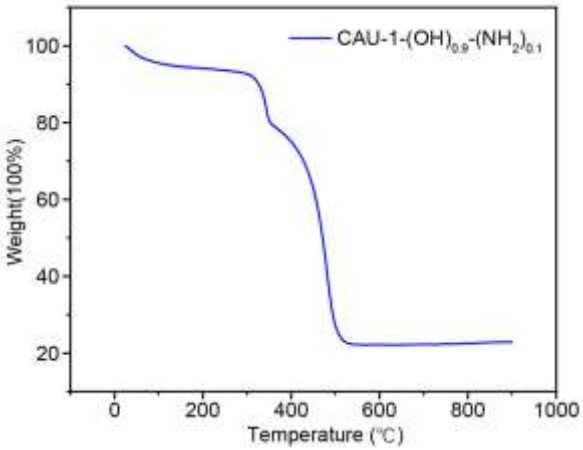

Figure S43. TGA trace of CAU-1-$(OH)_{0.9}$-$(NH_2)_{0.1}$.

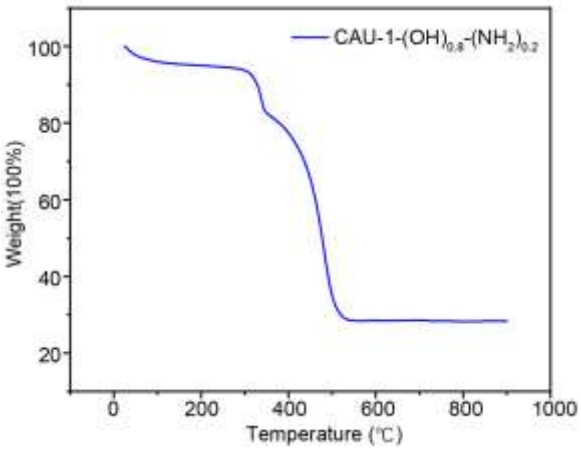

Figure S44. TGA trace of CAU-1-$(OH)_{0.8}$-$(NH_2)_{0.2}$.

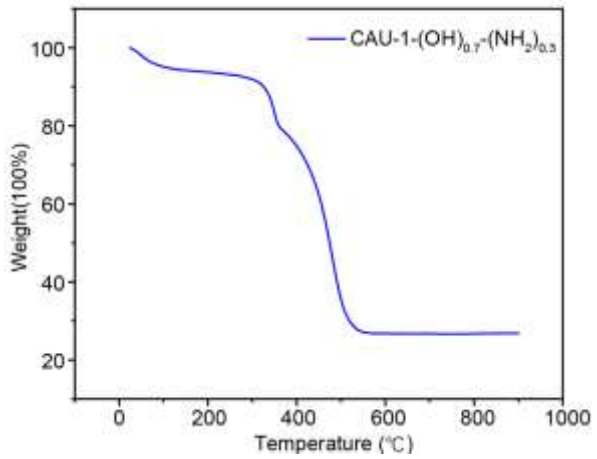

Figure S45. TGA trace of CAU-1-$(OH)_{0.7}$-$(NH_2)_{0.3}$.

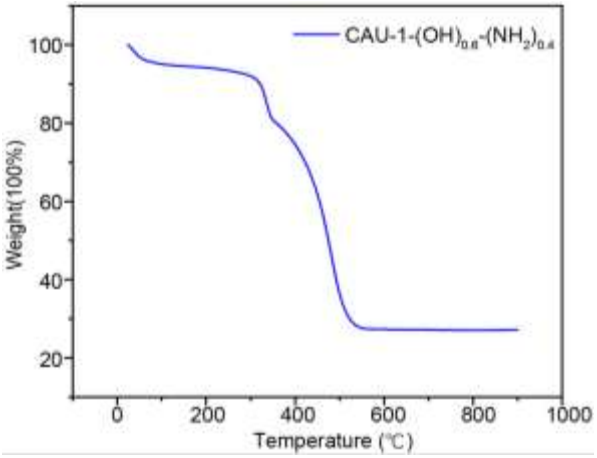

Figure S46. TGA trace of CAU-1-$(OH)_{0.6}$-$(NH_2)_{0.4}$.

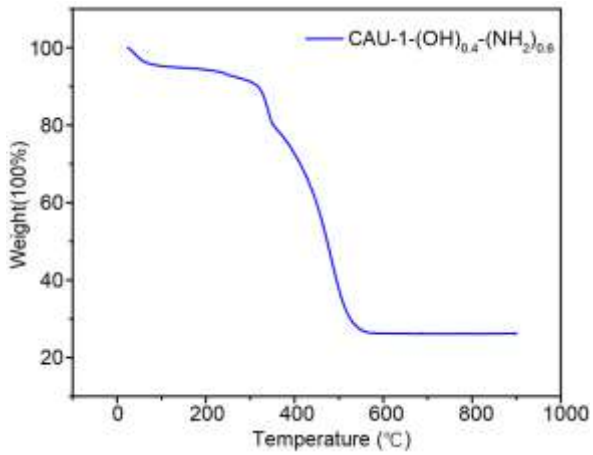

Figure S47. TGA trace of CAU-1-$(OH)_{0.4}$-$(NH_2)_{0.6}$.

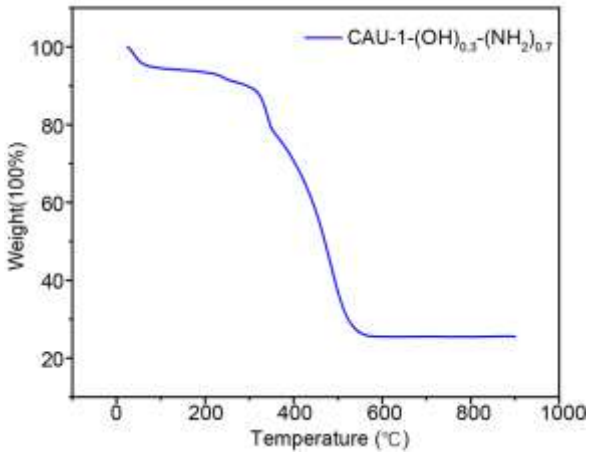

Figure S48. TGA trace of CAU-1-$(OH)_{0.3}$-$(NH_2)_{0.7}$.

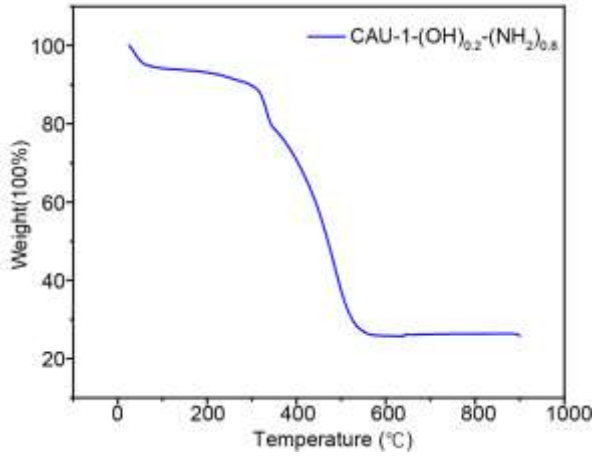

Figure S49. TGA trace of CAU-1-$(OH)_{0.2}$-$(NH_2)_{0.8}$.

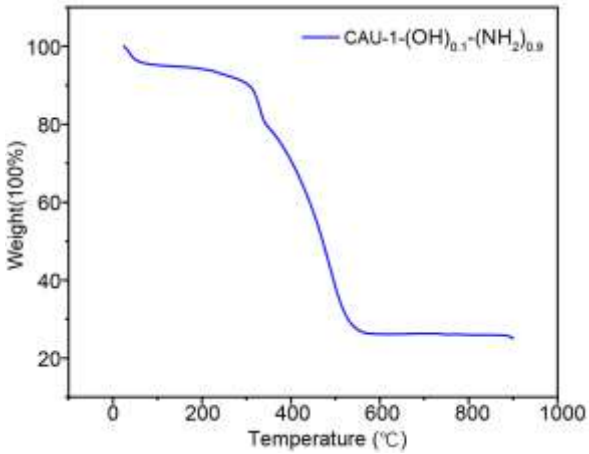

Figure S50. TGA trace of CAU-1-$(OH)_{0.1}$-$(NH_2)_{0.9}$.

8 Fourier transform infrared spectroscopy (FTIR)

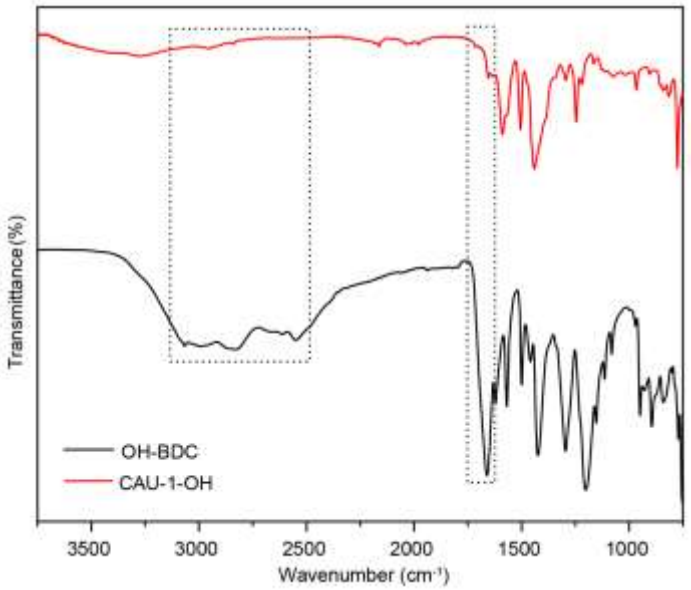

Figure S51. IR spectra of CAU-1-OH and OH-BDC.

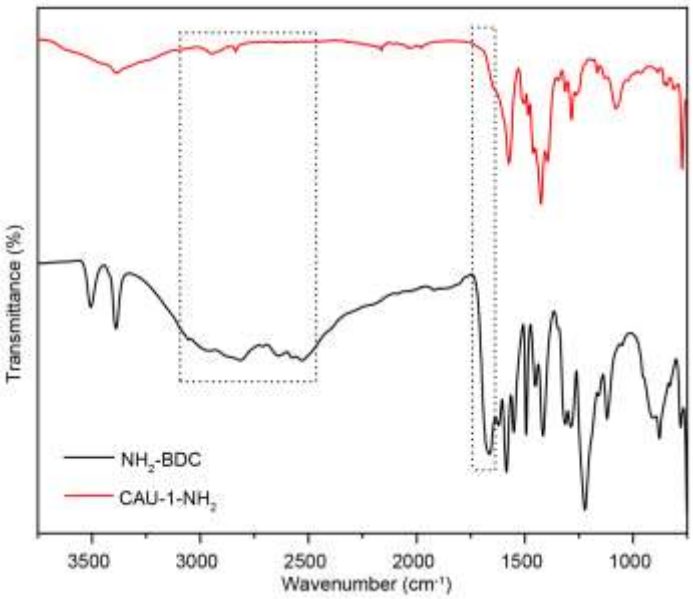

Figure S52. IR spectra of CAU-1-NH_2 and NH_2-BDC.

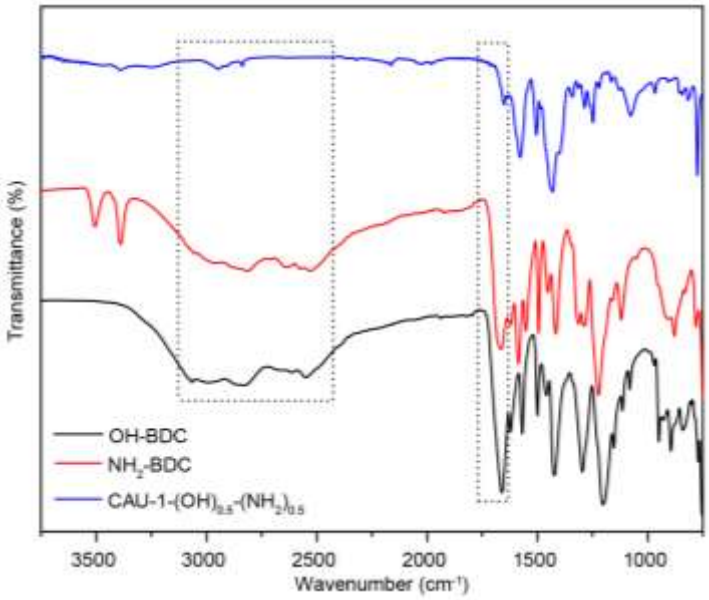

Figure S53. IR spectra of CAU-1-$(OH)_{0.5}$-$(NH_2)_{0.5}$, OH-BDC, and NH_2-BDC.

9 N_2 adsorption analysis

The drying and activation of MOF samples were carried out by vacuum heating degassing. After centrifugation, the precipitated sample was put into the degassing station after being dried in the double row tube with the adsorption tube. The heating procedure is set. The temperature was heated at 130 °C for 12 hours, and the temperature rise and fall rate is 1 °C per minute. At the same time, the vacuum degree of the degassing station is reduced to less than 10 Pa. After heating and degassing, the sample was analyzed in BELSORP-max (MicrotracBEL) at 77 K.

CAU-1-OH
Low crystallinity:

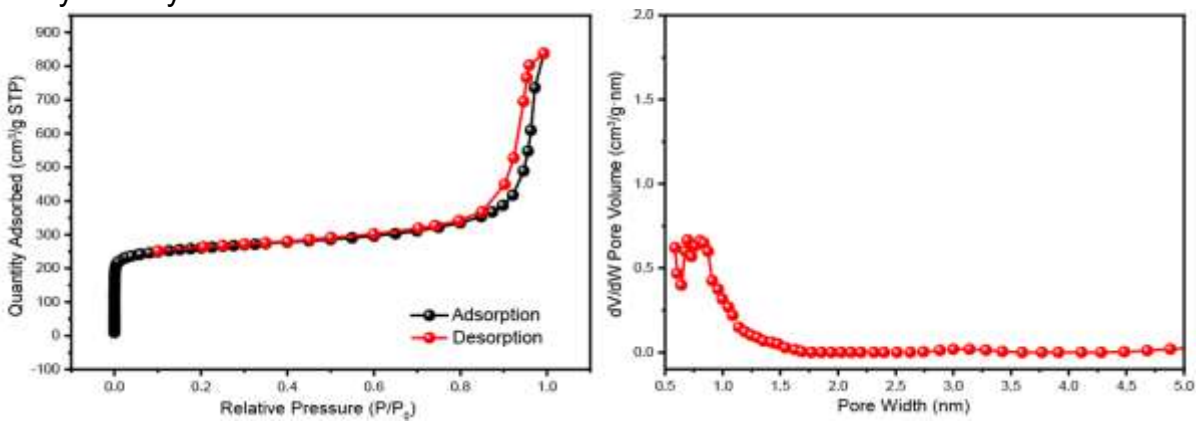

Figure S54. Nitrogen isotherm of low crystallinity CAU-1-OH at 77 K (left). Pore size distribution of low crystallinity CAU-1-OH (right).

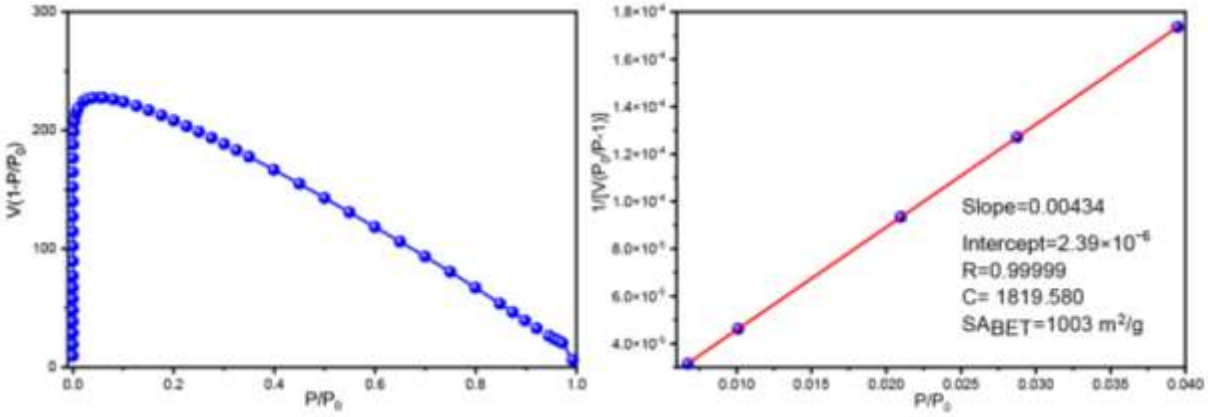

Figure S55. BET area calculation for CAU-1-OH of low crystallinity from nitrogen isotherm at 77 K (left). Plot of the linear P/P_0 range (right).

230 nm:

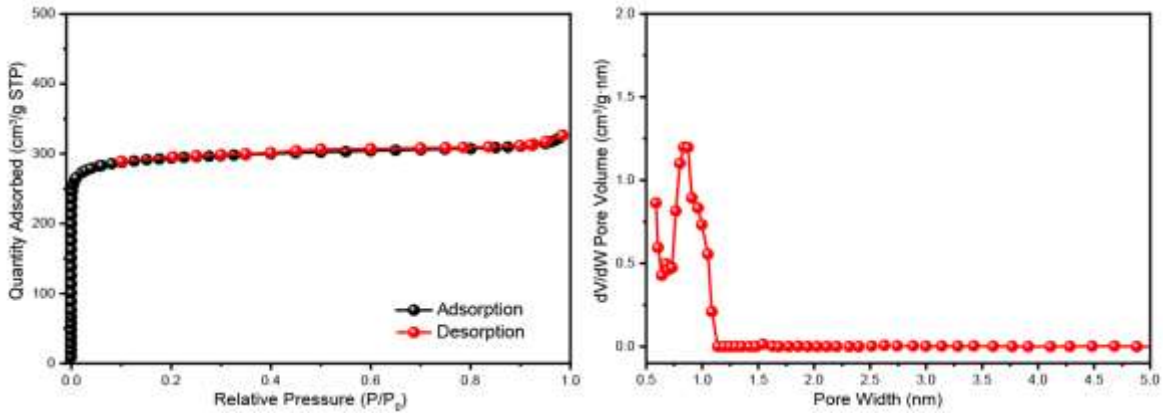

Figure S56. Nitrogen isotherm of 230 nm CAU-1-OH at 77 K (left). Pore size distribution of 230 nm CAU-1-OH (right).

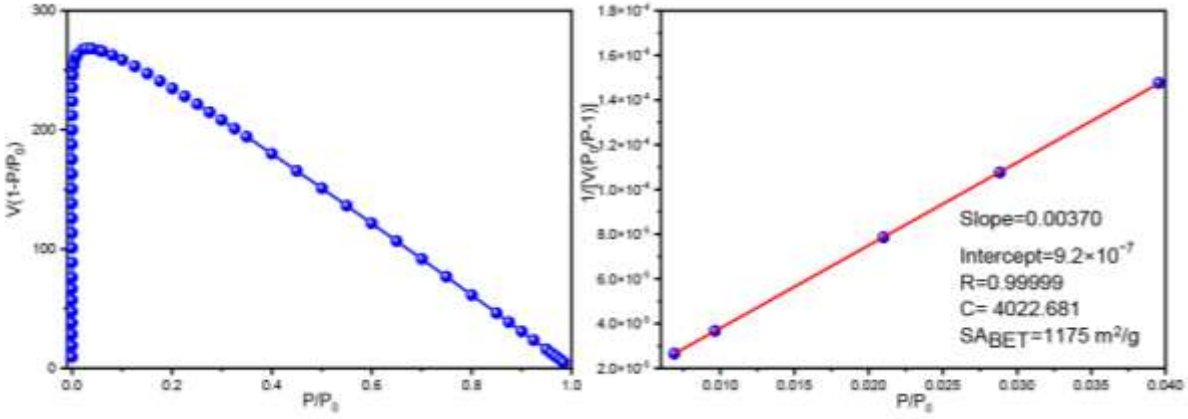

Figure S57. BET area calculation for CAU-1-OH at 230 nm from nitrogen isotherm at 77 K (left). Plot of the linear P/P_0 range (right).

550 nm:

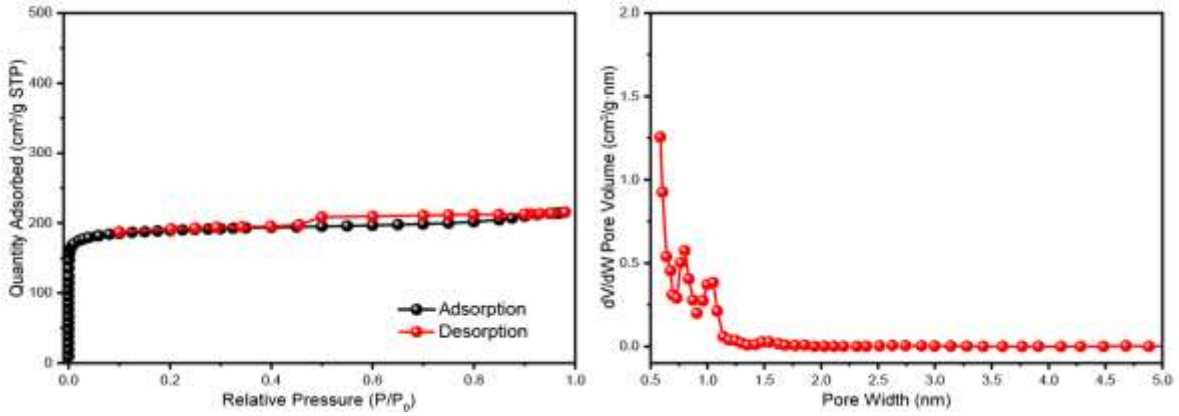

Figure S58. Nitrogen isotherm of 550 nm CAU-1-OH at 77 K (left). Pore size distribution of 550 nm CAU-1-OH (right).

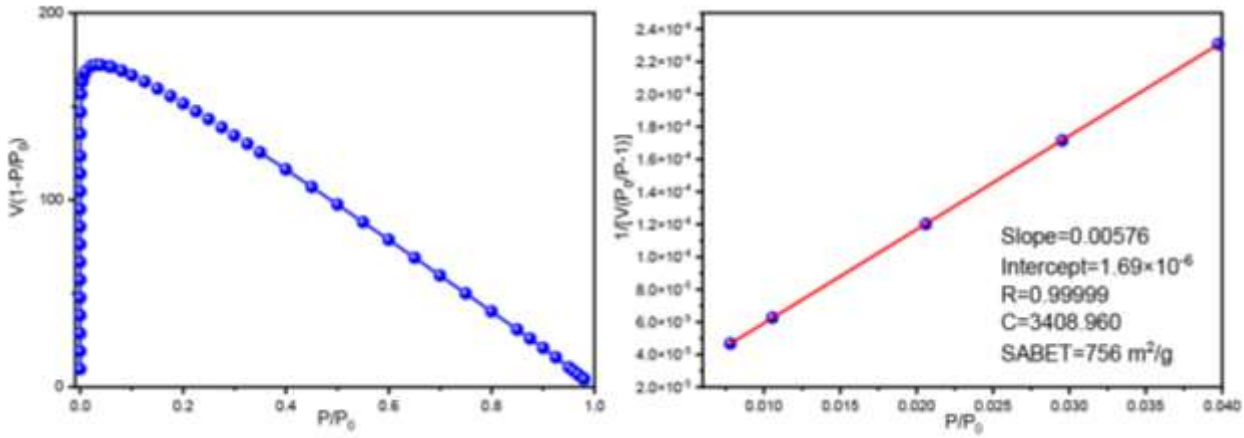

Figure S59. BET area calculation for CAU-1-OH at 550 nm from nitrogen isotherm at 77 K (left). Plot of the linear P/P_0 range (right).

800 nm:

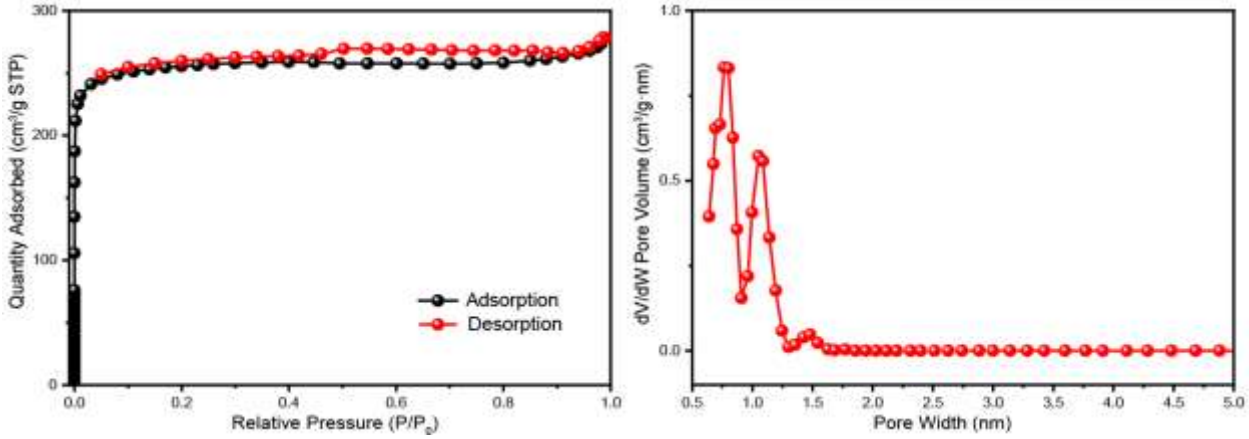

Figure S60. Nitrogen isotherm of 800 nm CAU-1-OH at 77 K (left). Pore size distribution of 800 nm CAU-1-OH (right).

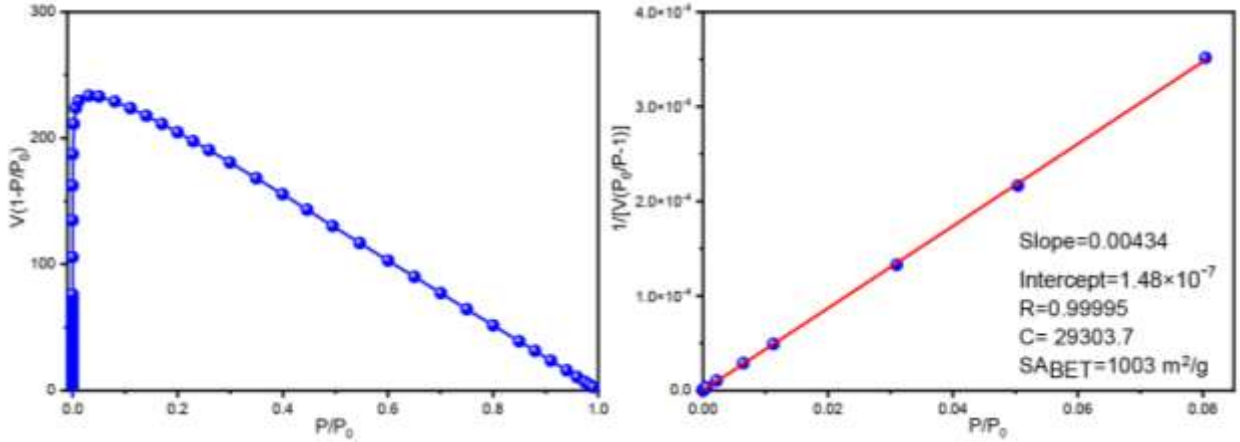

Figure S61. BET area calculation for CAU-1-OH of 800 nm from nitrogen isotherm at 77 K (left). Plot of the linear P/P_0 range (right).

CAU-1-NH_2
Low crystallinity:

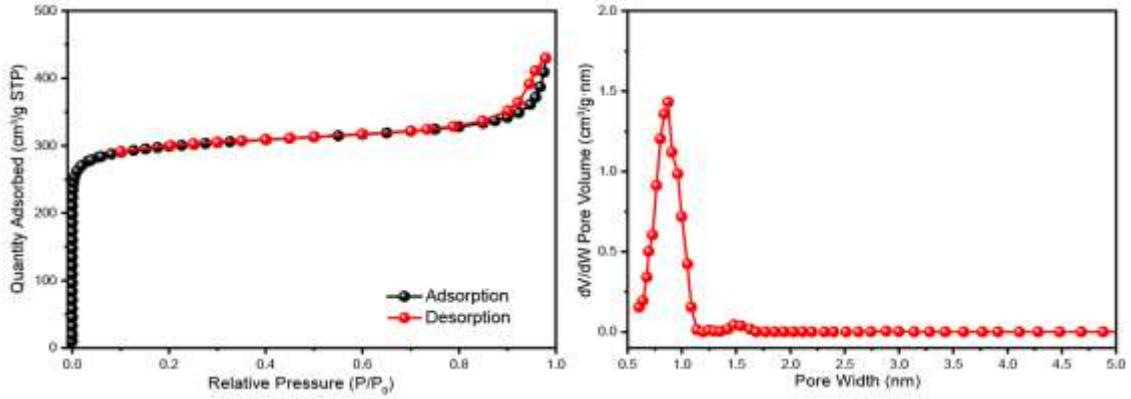

Figure S62. Nitrogen isotherm of low crystallinity CAU-1-NH_2 at 77 K (left). Pore size distribution of low crystallinity CAU-1-NH_2 (right).

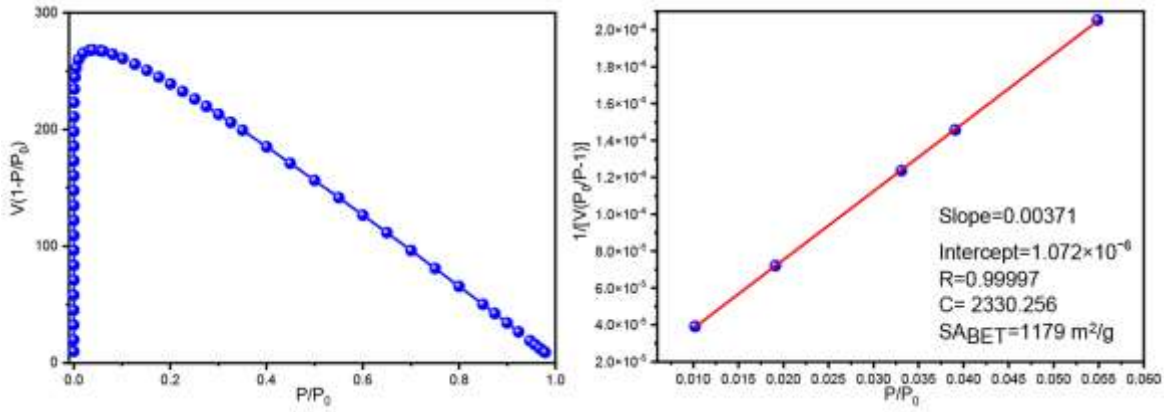

Figure S63. BET area calculation for CAU-1-NH_2 of low crystallinity from nitrogen isotherm at 77 K (left). Plot of the linear P/P_0 range (right).

210 nm:

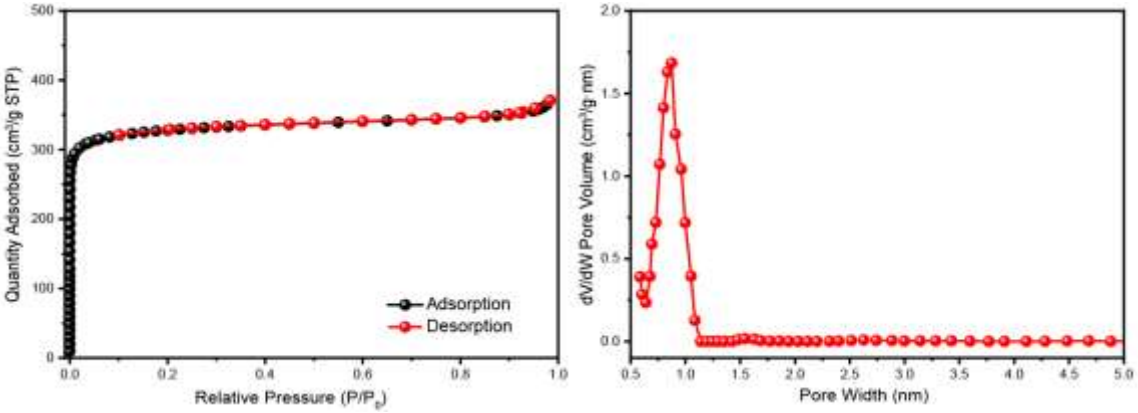

Figure S64. Nitrogen isotherm of 210 nm CAU-1-NH_2 at 77 K (left). Pore size distribution of 210 nm CAU-1-NH_2 (right).

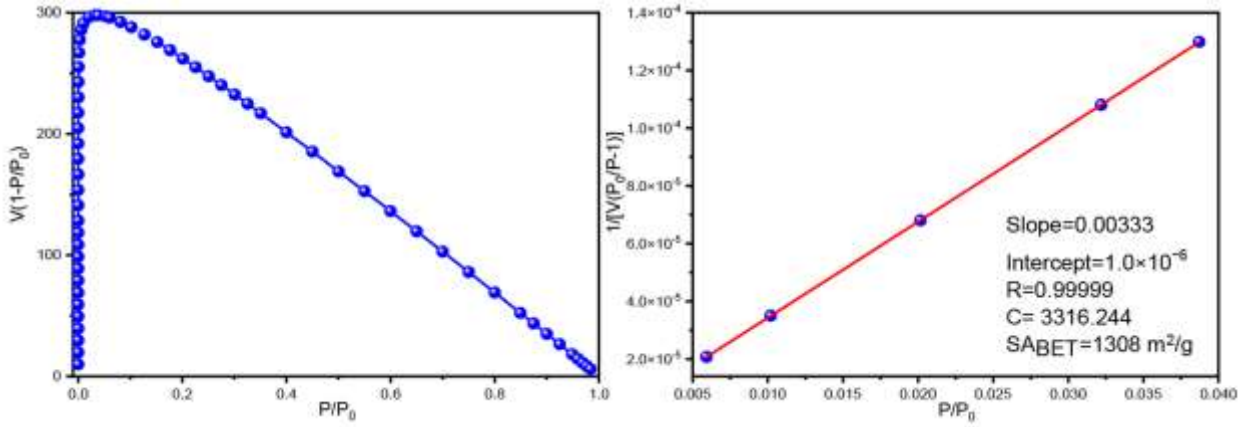

Figure S65. BET area calculation for CAU-1-NH_2 of 210 nm from nitrogen isotherm at 77 K (left). Plot of the linear *P*/*P*0 range (right).

300 nm:

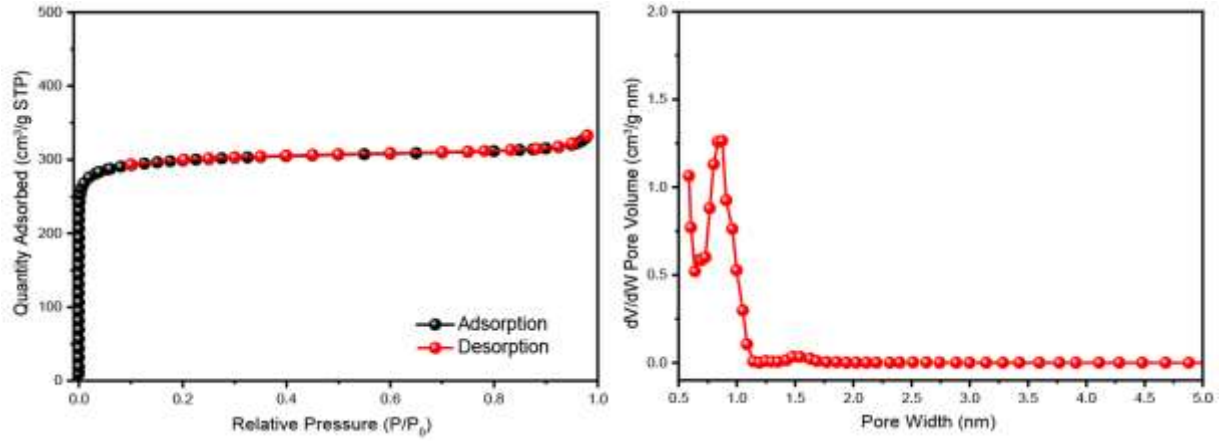

Figure S66. Nitrogen isotherm of 300 nm CAU-1-NH_2 at 77 K (left). Pore size distribution of 300 nm CAU-1-NH_2 (right).

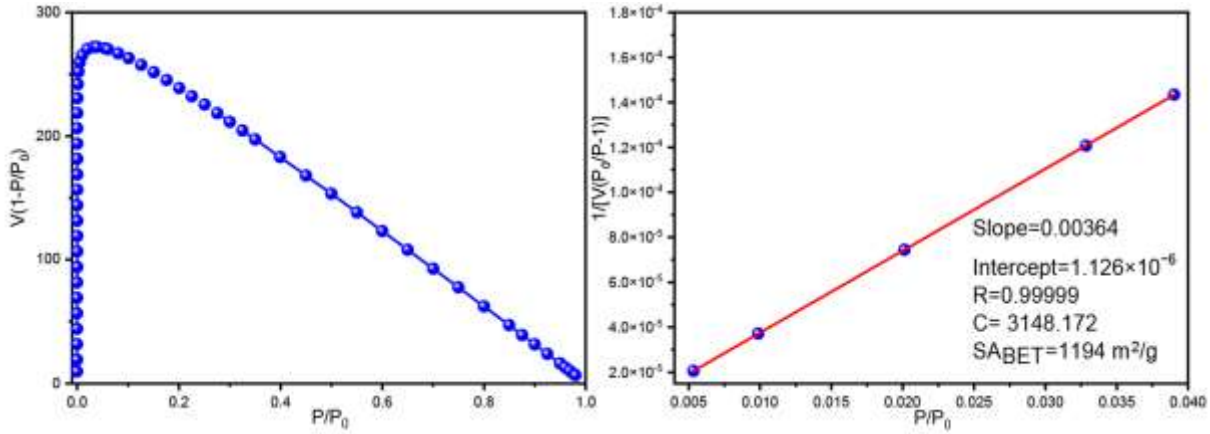

Figure S67. BET area calculation for CAU-1-NH_2 of 300 nm from nitrogen isotherm at 77 K (left). Plot of the linear *P*/*P*0 range (right).

900 nm:

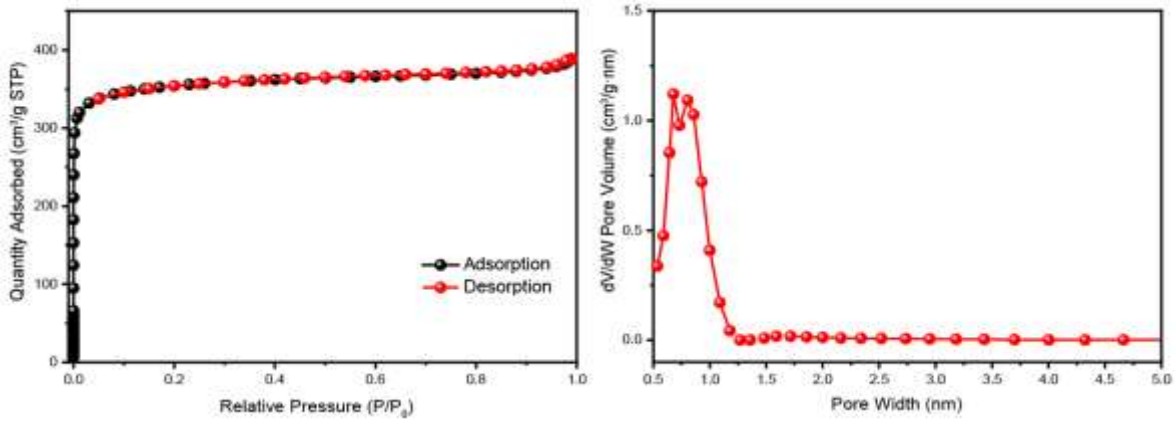

Figure S68. Nitrogen isotherm of 900 nm CAU-1-NH_2 at 77 K (left). Pore size distribution of 900 nm CAU-1-NH_2 (right).

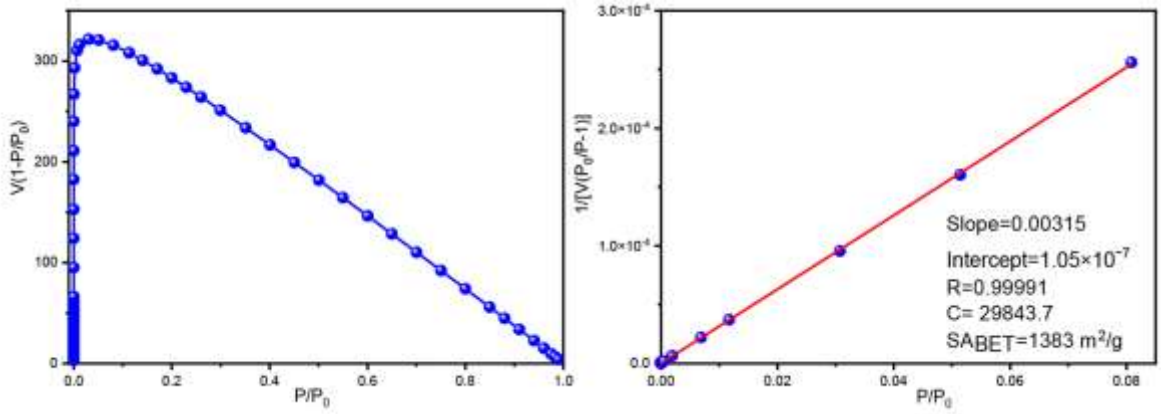

Figure S69. BET area calculation for CAU-1-NH_2 of 900 nm from nitrogen isotherm at 77 K (left). Plot of the linear *P/P*0 range (right).

CAU-1-$(OH)_{0.5}$-$(NH_2)_{0.5}$
35 nm:

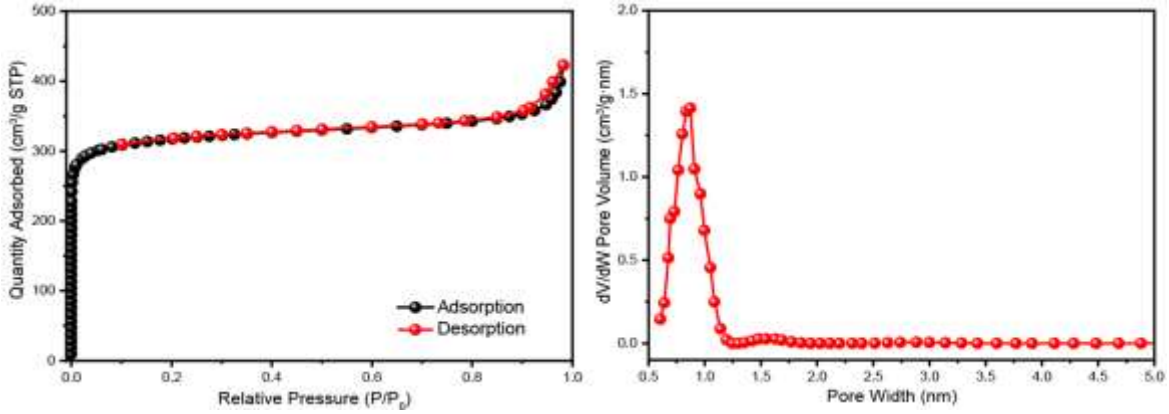

Figure S70. Nitrogen isotherm of 35 nm CAU-1-$(OH)_{0.5}$-$(NH_2)_{0.5}$ at 77 K (left). Pore size distribution of 35 nm CAU-1-$(OH)_{0.5}$-$(NH_2)_{0.5}$ (right).

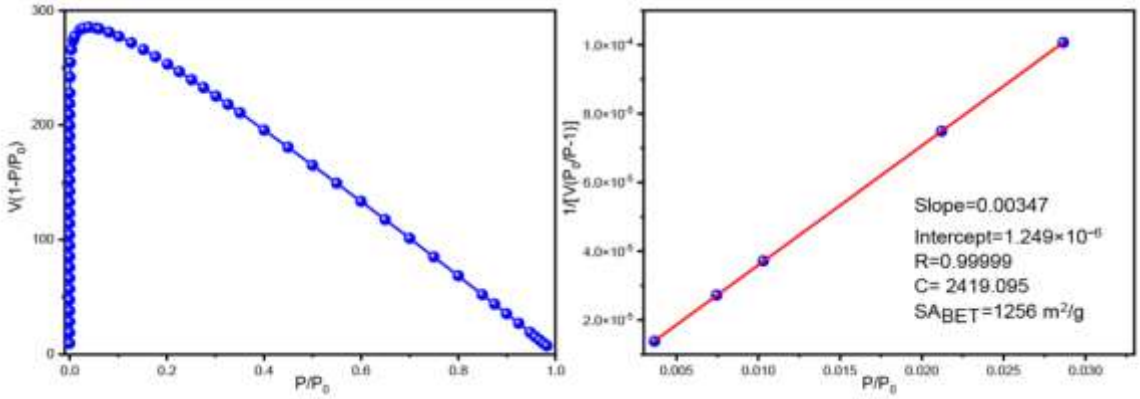

Figure S71. BET area calculation for CAU-1-$(OH)_{0.5}$-$(NH_2)_{0.5}$ of 35 nm from nitrogen isotherm at 77 K (left). Plot of the linear P/P_0 range (right).

200 nm:

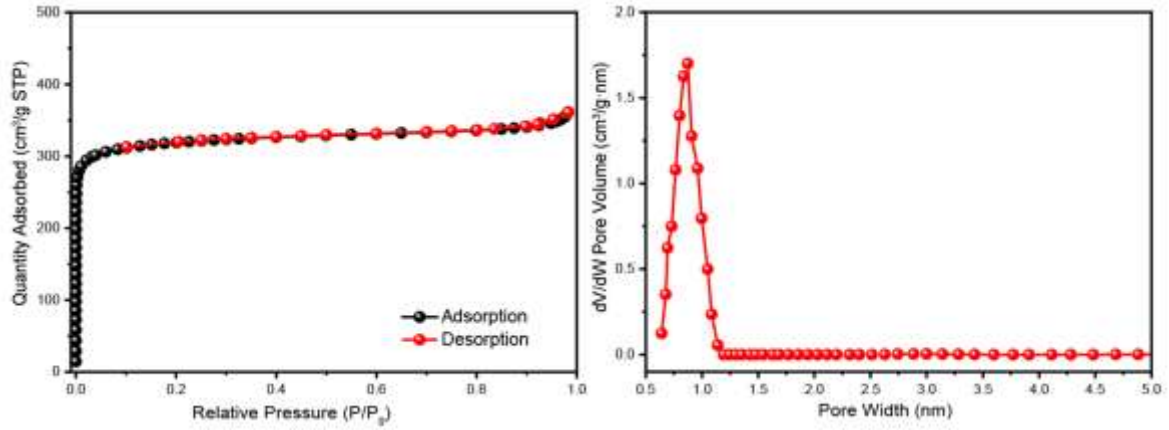

Figure S72. Nitrogen isotherm of 200 nm CAU-1-$(OH)_{0.5}$-$(NH_2)_{0.5}$ at 77 K (left). Pore size distribution of 200 nm CAU-1-$(OH)_{0.5}$-$(NH_2)_{0.5}$ (right).

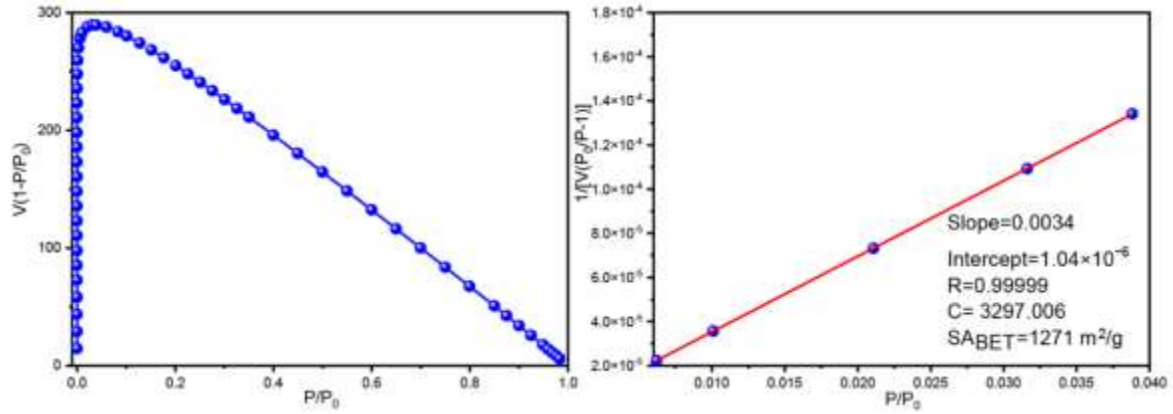

Figure S73. BET area calculation for CAU-1-$(OH)_{0.5}$-$(NH_2)_{0.5}$ of 200 nm from nitrogen isotherm at 77 K (left). Plot of the linear *P*/*P*0 range (right).

650 nm:

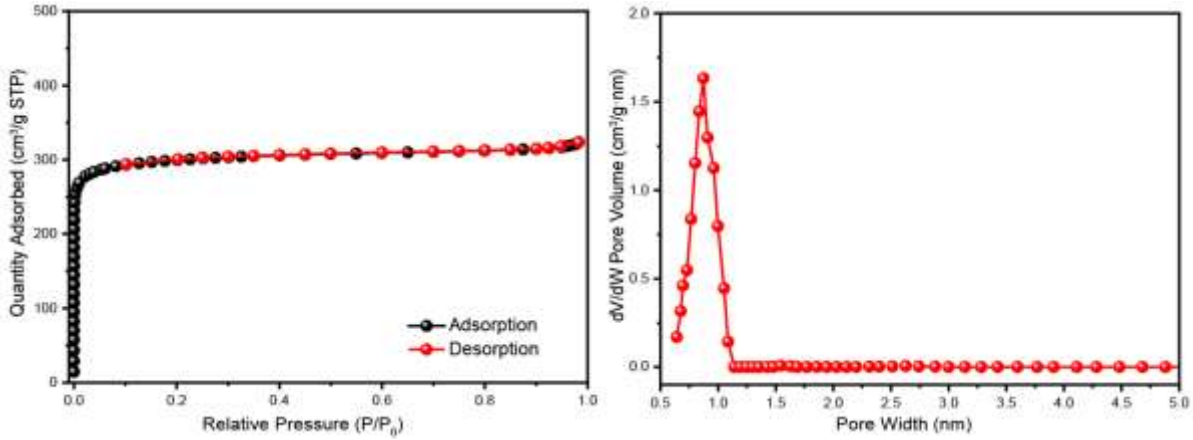

Figure S74. Nitrogen isotherm of 650 nm CAU-1-$(OH)_{0.5}$-$(NH_2)_{0.5}$ at 77 K (left). Pore size distribution of 650 nm CAU-1-$(OH)_{0.5}$-$(NH_2)_{0.5}$ (right).

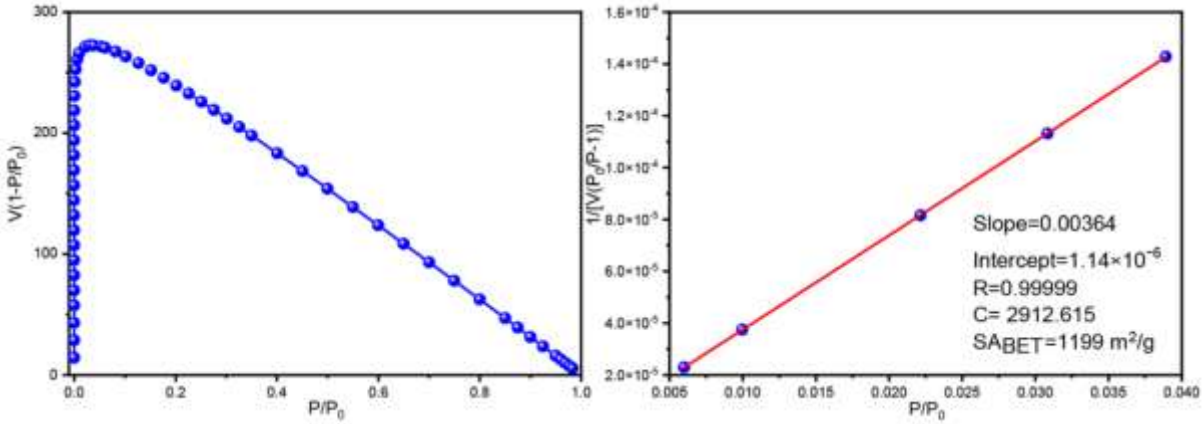

Figure S75. BET area calculation for CAU-1-$(OH)_{0.5}$-$(NH_2)_{0.5}$ of 650 nm from nitrogen isotherm at 77 K (left). Plot of the linear *P*/*P*0 range (right).

900 nm:

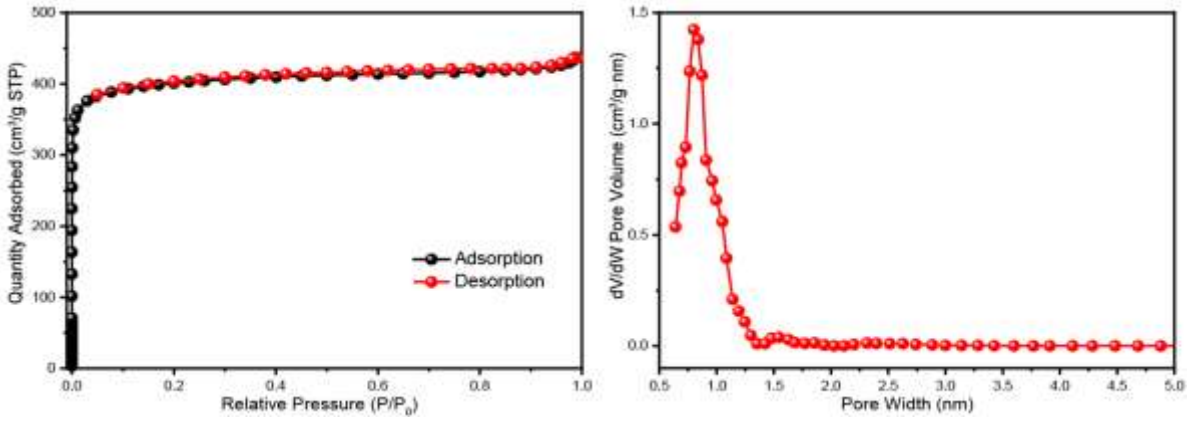

Figure S76. Nitrogen isotherm of 900 nm CAU-1-$(OH)_{0.5}$-$(NH_2)_{0.5}$ at 77 K (left). Pore size distribution of 900 nm CAU-1-$(OH)_{0.5}$-$(NH_2)_{0.5}$ (right).

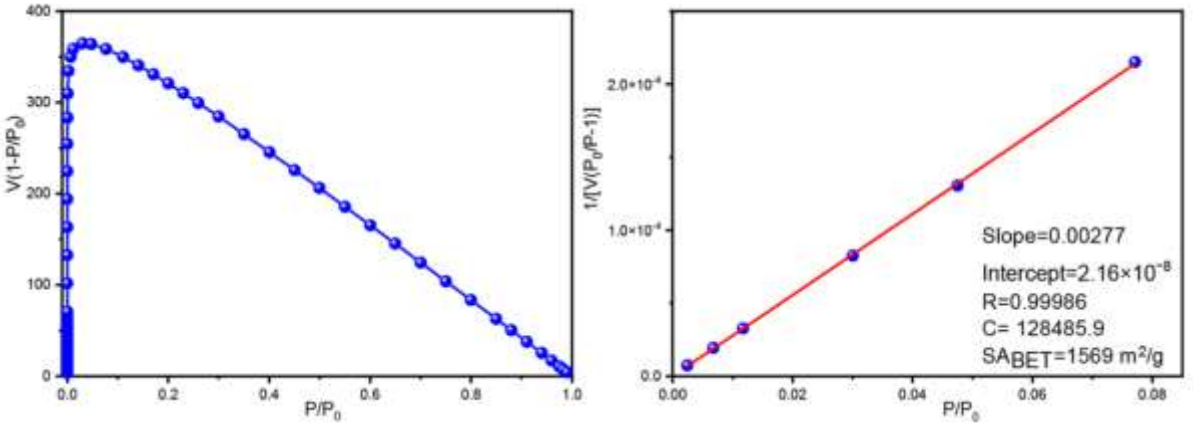

Figure S77. BET area calculation for CAU-1-$(OH)_{0.5}$-$(NH_2)_{0.5}$ of 900 nm from nitrogen isotherm at 77 K (left). Plot of the linear P/P_0 range (right).

Different ligand ratios:

CAU-1-$(OH)_{0.9}$-$(NH_2)_{0.1}$:

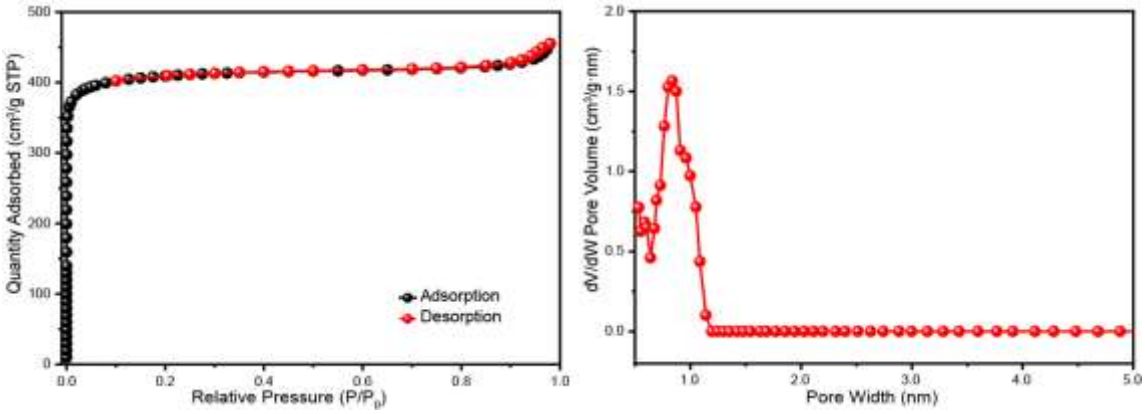

Figure S78. Nitrogen isotherm of CAU-1-$(OH)_{0.9}$-$(NH_2)_{0.1}$ at 77 K (left). Pore size distribution of CAU-1-$(OH)_{0.9}$-$(NH_2)_{0.1}$ (right).

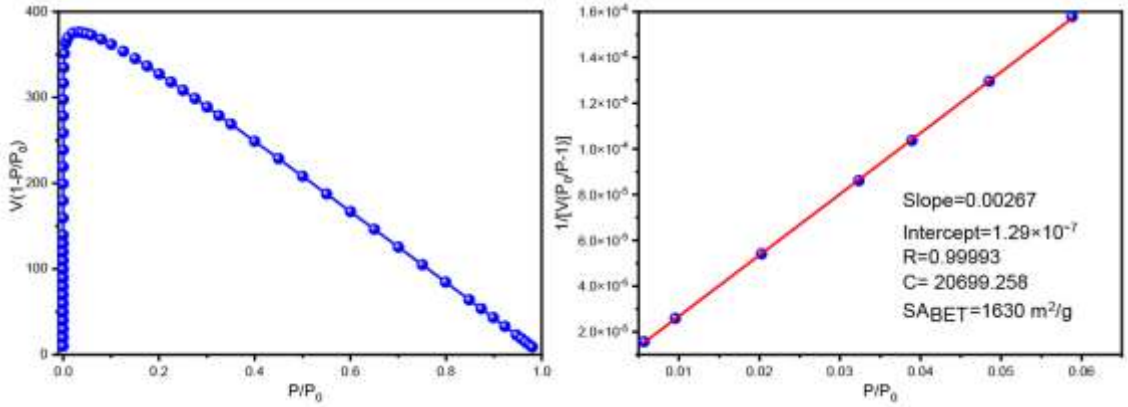

Figure S79. BET area calculation for CAU-1-$(OH)_{0.9}$-$(NH_2)_{0.1}$ from nitrogen isotherm at 77 K (left). Plot of the linear P/P_0 range (right).

CAU-1-$(OH)_{0.8}$-$(NH_2)_{0.2}$:

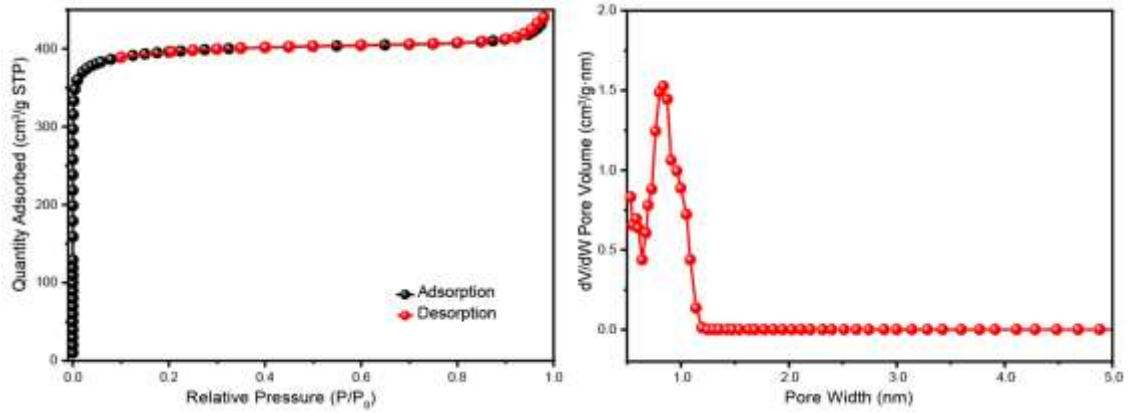

Figure S80. Nitrogen isotherm of CAU-1-$(OH)_{0.8}$-$(NH_2)_{0.2}$ at 77 K (left). Pore size distribution of CAU-1-$(OH)_{0.8}$-$(NH_2)_{0.2}$ (right).

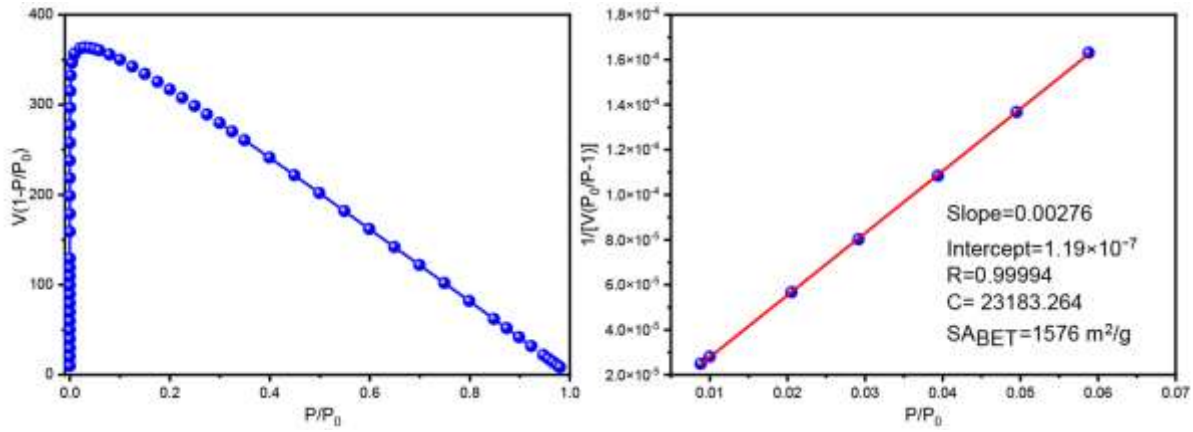

Figure S81. BET area calculation for CAU-1-$(OH)_{0.8}$-$(NH_2)_{0.2}$ from nitrogen isotherm at 77 K (left). Plot of the linear P/P_0 range (right).

CAU-1-$(OH)_{0.7}$-$(NH_2)_{0.3}$:

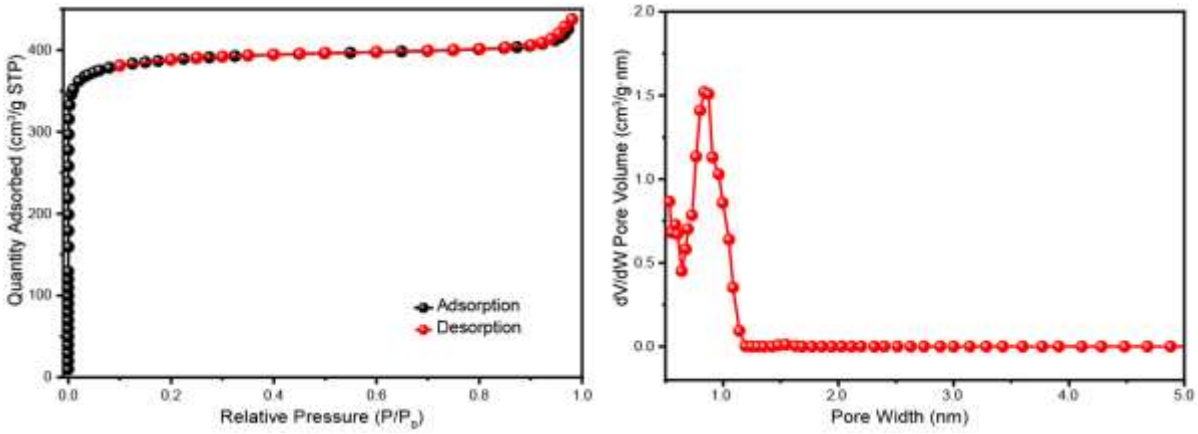

Figure S82. Nitrogen isotherm of CAU-1-$(OH)_{0.7}$-$(NH_2)_{0.3}$ at 77 K (left). Pore size distribution of CAU-1-$(OH)_{0.7}$-$(NH_2)_{0.3}$ (right).

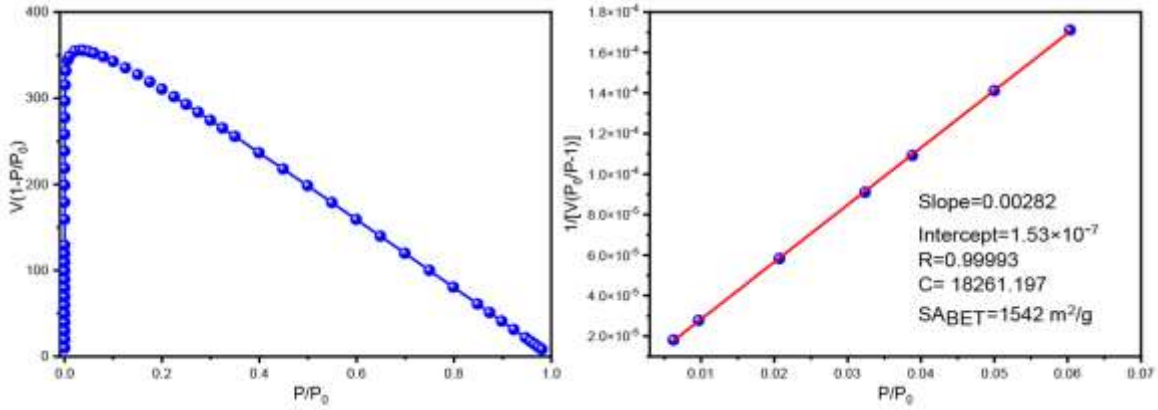

Figure S83. BET area calculation for CAU-1-$(OH)_{0.7}$-$(NH_2)_{0.3}$ from nitrogen isotherm at 77 K (left). Plot of the linear P/P_0 range (right).

CAU-1-$(OH)_{0.6}$-$(NH_2)_{0.4}$:

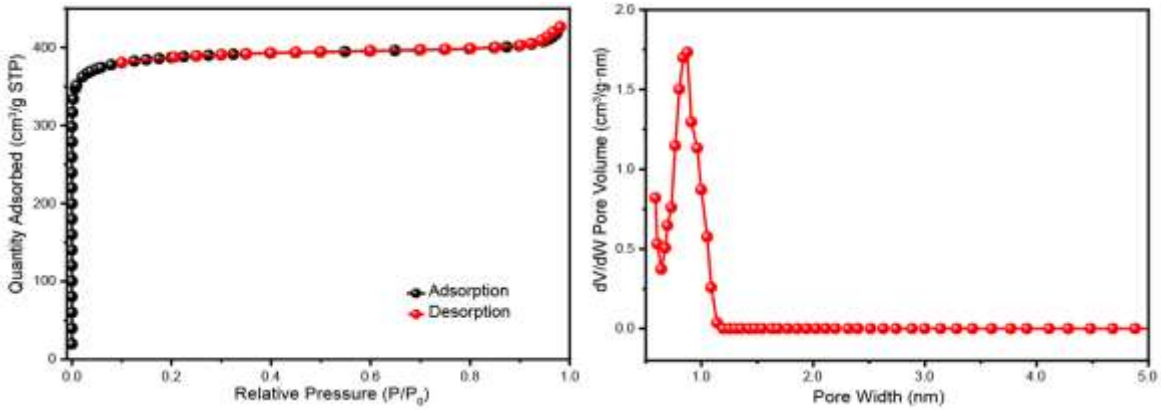

Figure S84. Nitrogen isotherm of CAU-1-$(OH)_{0.6}$-$(NH_2)_{0.4}$ at 77 K (left). Pore size distribution of CAU-1-$(OH)_{0.6}$-$(NH_2)_{0.4}$ (right).

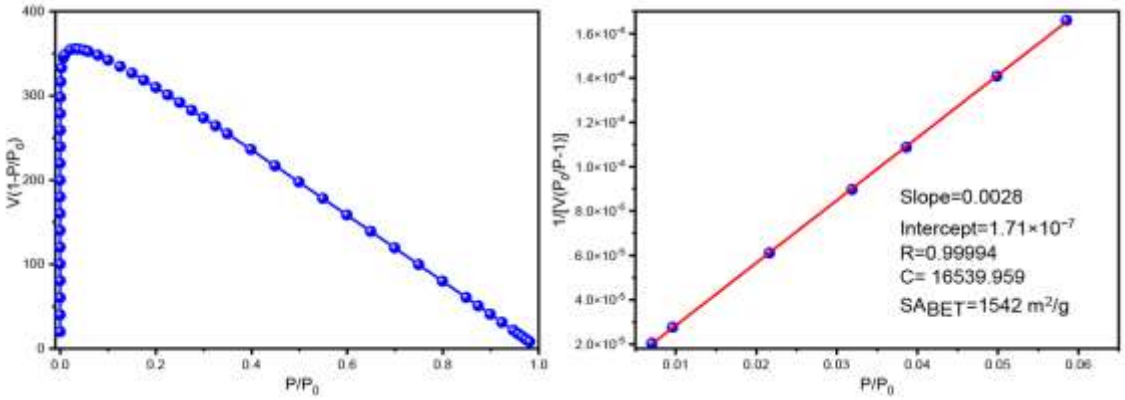

Figure S85. BET area calculation for CAU-1-$(OH)_{0.6}$-$(NH_2)_{0.4}$ from nitrogen isotherm at 77 K (left). Plot of the linear P/P_0 range (right).

CAU-1-$(OH)_{0.4}$-$(NH_2)_{0.6}$:

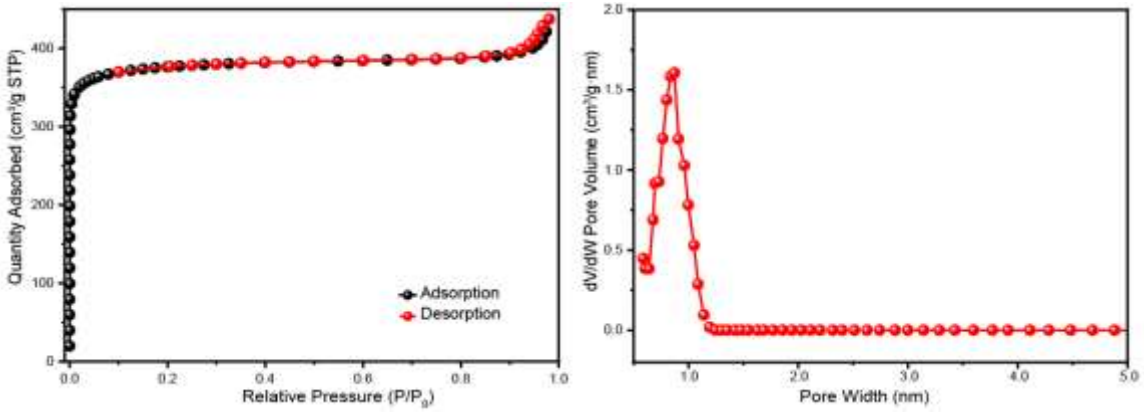

Figure S86. Nitrogen isotherm of CAU-1-$(OH)_{0.4}$-$(NH_2)_{0.6}$ at 77 K (left). Pore size distribution of CAU-1-$(OH)_{0.4}$-$(NH_2)_{0.6}$ (right).

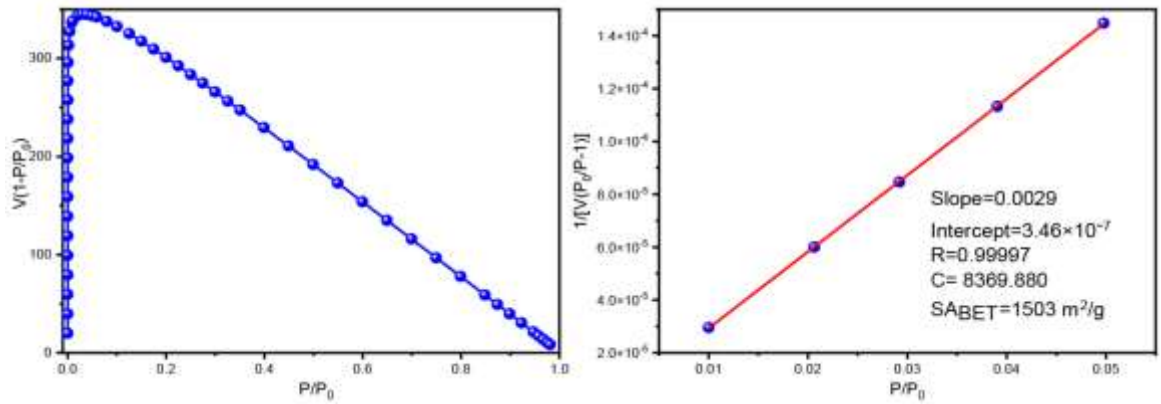

Figure S87. BET area calculation for CAU-1-$(OH)_{0.4}$-$(NH_2)_{0.6}$ from nitrogen isotherm at 77 K (left). Plot of the linear *P*/*P*0 range (right).

CAU-1-$(OH)_{0.3}$-$(NH_2)_{0.7}$:

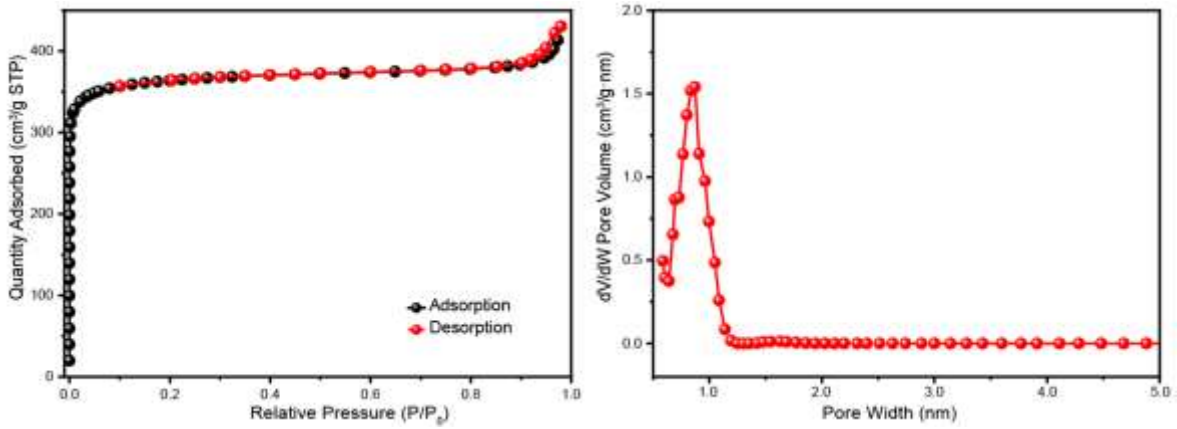

Figure S88. Nitrogen isotherm of CAU-1-$(OH)_{0.3}$-$(NH_2)_{0.7}$ at 77 K (left). Pore size distribution of CAU-1-$(OH)_{0.3}$-$(NH_2)_{0.7}$ (right).

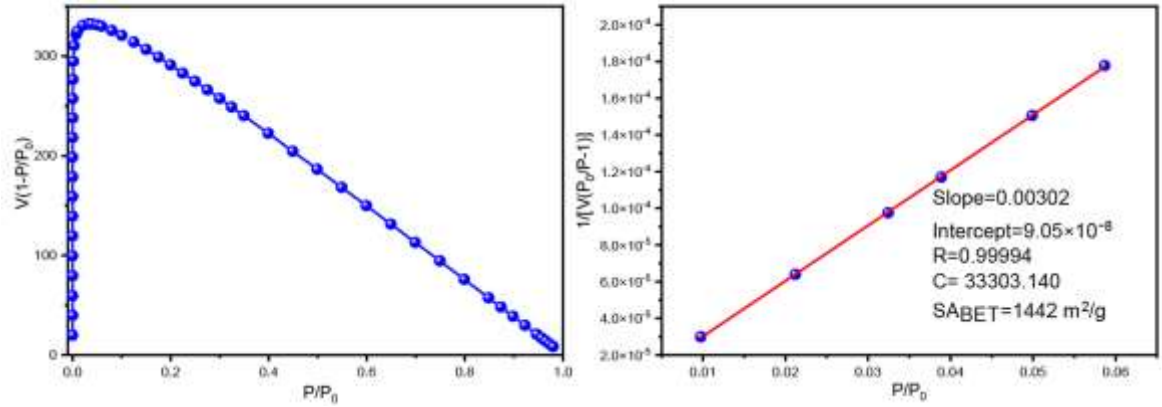

Figure S89. BET area calculation for CAU-1-$(OH)_{0.3}$-$(NH_2)_{0.7}$ from nitrogen isotherm at 77 K (left). Plot of the linear *P*/*P*0 range (right).

CAU-1-$(OH)_{0.2}$-$(NH_2)_{0.8}$:

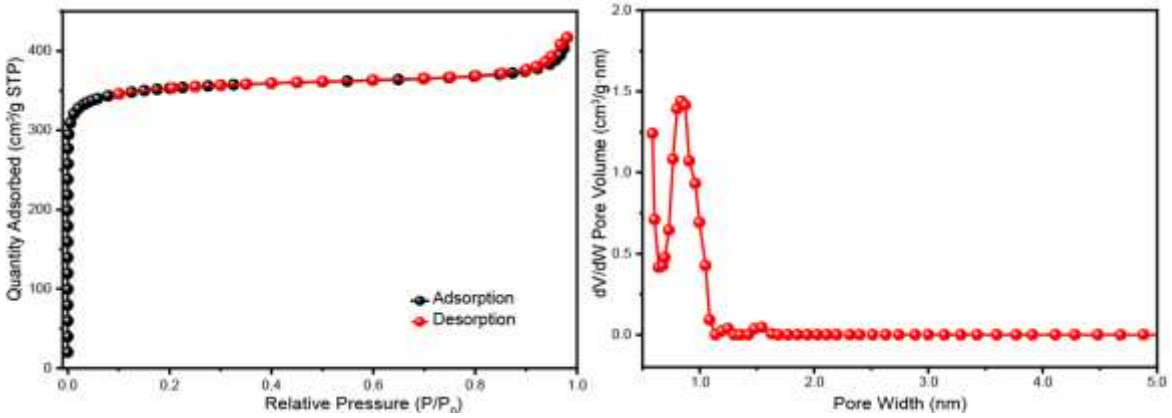

Figure S90. Nitrogen isotherm of CAU-1-$(OH)_{0.2}$-$(NH_2)_{0.8}$ at 77 K (left). Pore size distribution of CAU-1-$(OH)_{0.2}$-$(NH_2)_{0.8}$ (right).

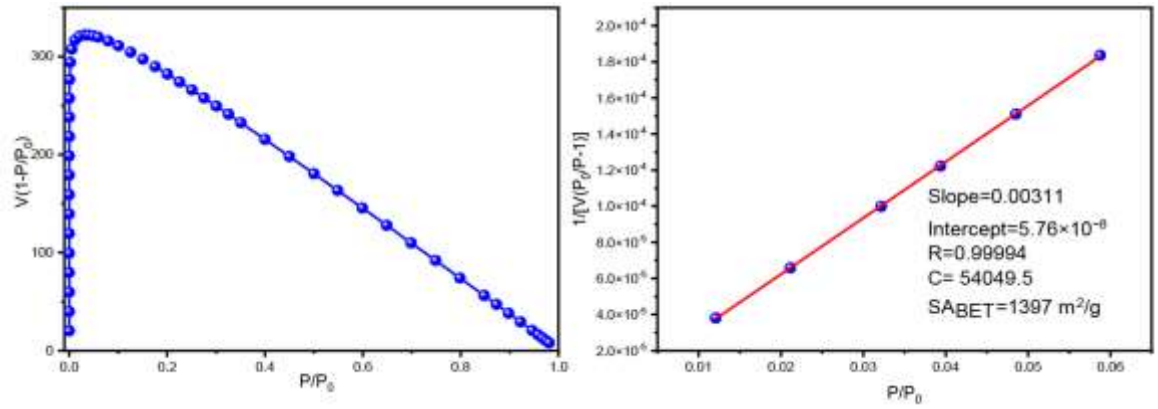

Figure S91. BET area calculation for CAU-1-$(OH)_{0.2}$-$(NH_2)_{0.8}$ from nitrogen isotherm at 77 K (left). Plot of the linear P/P_0 range (right).

CAU-1-$(OH)_{0.1}$-$(NH_2)_{0.9}$:

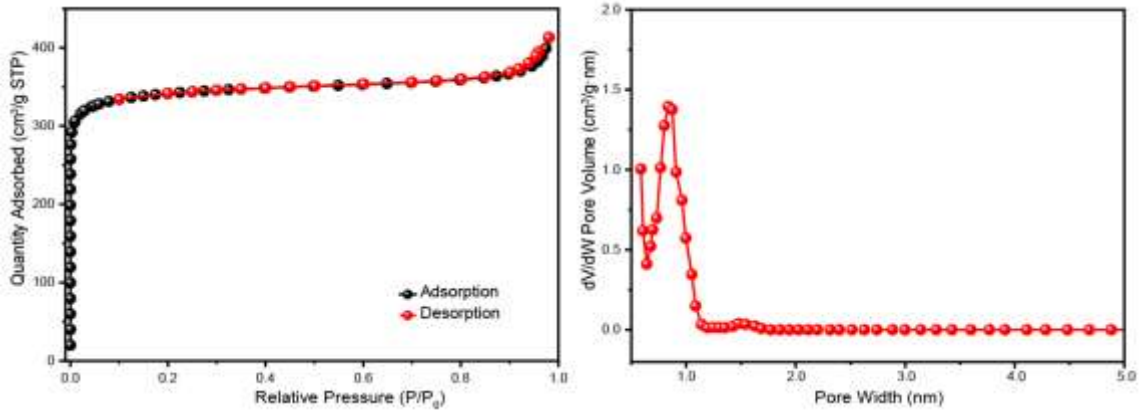

Figure S92. Nitrogen isotherm of CAU-1-$(OH)_{0.1}$-$(NH_2)_{0.9}$ at 77 K (left). Pore size distribution of CAU-1-$(OH)_{0.1}$-$(NH_2)_{0.9}$ (right).

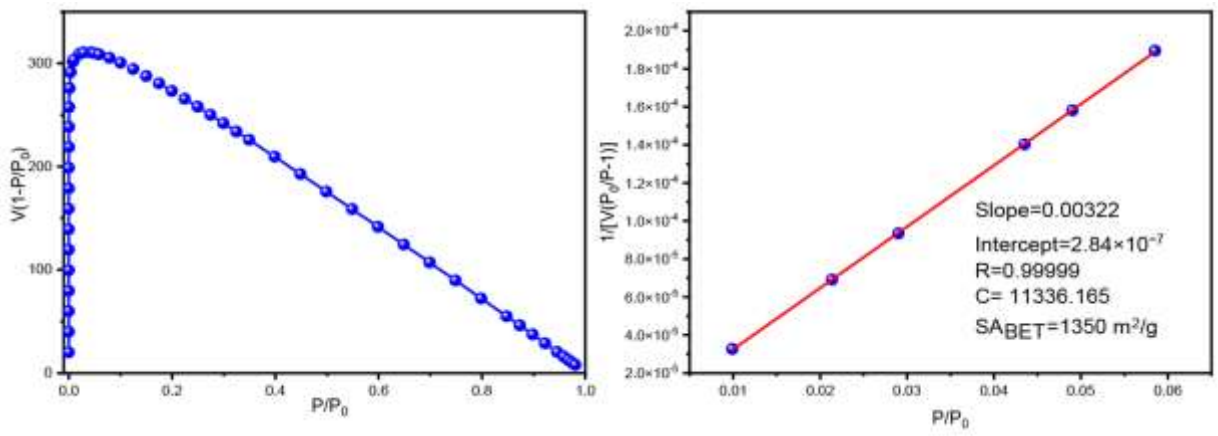

Figure S93. BET area calculation for CAU-1-$(OH)_{0.1}$-$(NH_2)_{0.9}$ from nitrogen isotherm at 77 K (left). Plot of the linear P/P_0 range (right).

10 Xe adsorption analysis and isosteric heat of adsorption

Xe adsorption/desorption isotherms were performed on a Micromeritics 3 Flex automatic volumetric instrument. Before the isotherm measurement, MOF powders were degassed on 3 Flex for 10 h at 120 °C. The analysis temperature was kept at 273 K and 298 K, respectively.

Isosteric heat of adsorption (Q_{st}) is used to evaluate the adsorption affinity of the gas molecules to the adsorbent material. Higher Q_{st} stands for stronger interactions between the adsorbate molecules and the adsorbent. The Clausius-Clapeyron equation was employed to calculate the Q_{st}:

$$Q_{st} = -RT^2 \left(\frac{\partial lnP}{\partial T}\right)_{n_a}$$

Where n_a (mmol/g) is the amount of adsorbed gas, T (K) is the temperature, P (kPa) is the pressure, Q_{st} (kJ/mol) is the isosteric heat of adsorption. Integration of the equation gives:

$$lnP = \frac{Q_{st}}{RT} + C$$

In this study, adsorption equilibrium data at 298 and 273 K were used to estimate the heat of adsorption. The heat of adsorption at a given uptake was calculated from the slopes of the isosteres according to the equations as mentioned.

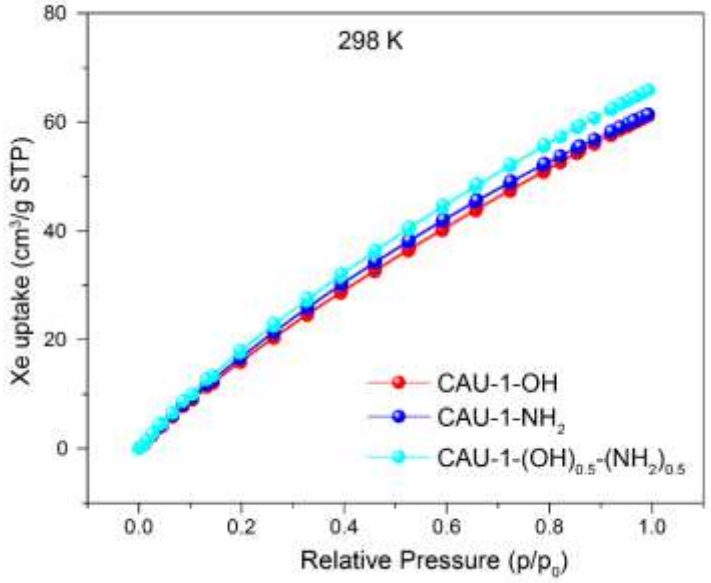

Figure S94. Xe adsorption isotherms of CAU-1-OH, CAU-1-NH_2, and CAU-1-$(OH)_{0.5}$-$(NH_2)_{0.5}$ at 298 K.

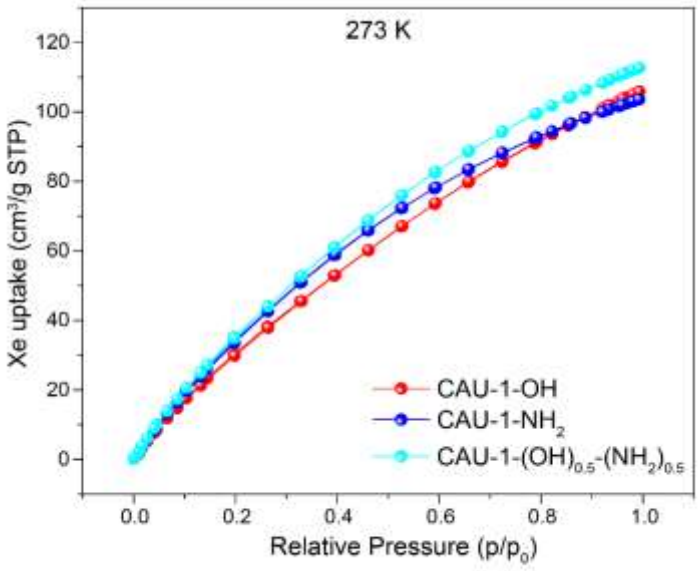

Figure S95. Xe adsorption isotherms of CAU-1-OH, CAU-1-NH_2, and CAU-1-$(OH)_{0.5}$-$(NH_2)_{0.5}$ at 273 K.

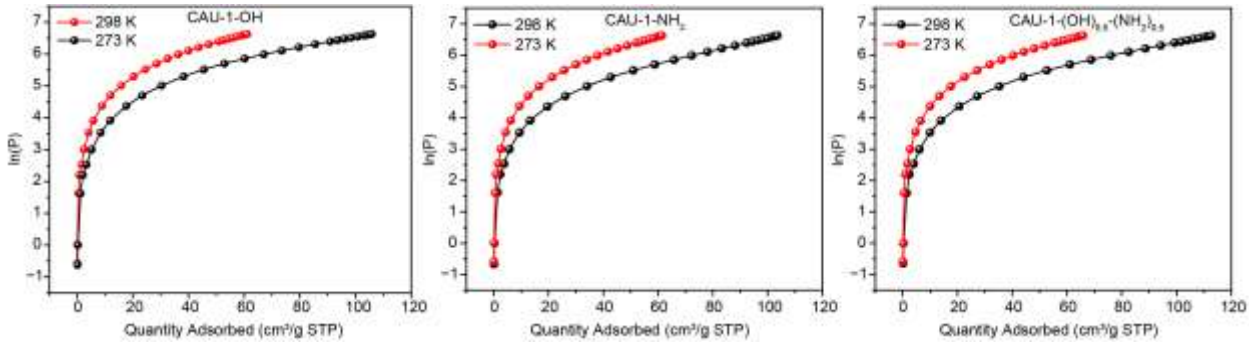

Figure S96. Virial fitting of the Xe adsorption isotherms for CAU-1-OH, CAU-1-NH_2, and CAU-1-$(OH)_{0.5}$-$(NH_2)_{0.5}$.

11 Computational details

All calculations were performed using density functional theory (DFT) with the projector augmented plane-wave method in the Vienna ab initio simulation package [1]. The exchange-correlation potential was approximated using the generalized gradient approximation (GGA) of Perdew, Burke, and Ernzerhof (PBE) [2], augmented with van der Waals (vdW) corrections implemented via the DFT-D3 method, incorporating the Becke and Johnson (BJ) damping scheme [3]. For structural optimization, a cutoff energy of 400 eV and a reduced k-point grid of 1×1×1 were adopted, ensuring total energy convergence to 1.0×10^{-5} eV and force convergence to 0.05 eV/Å.

The adsorption energy $E(\mathrm{ad})$ of the Xe atom on the MOF is defined as:

$$E(\mathrm{ad}) = E(\mathrm{MOF} + \mathrm{Xe}) - E(\mathrm{MOF}) - E(\mathrm{Xe})$$

Where $E(\mathrm{MOF} + \mathrm{Xe})$, $E(\mathrm{MOF})$ and $E(\mathrm{Xe})$ represent the total energies of the relaxed MOF with the adsorbed Xe, the isolated MOF, and the isolated Xe atom, respectively.

12 Hyperpolarized ^{129}Xe NMR spectra

Hyperpolarized ^{129}Xe gas was produced by a home-built ^{129}Xe hyperpolarizer. A gas mixture of 10% N_2, 88% He, and 2% Xe (naturally abundant ^{129}Xe) was flowed through a home-made hyperpolarizer (hyperpolarized ^{129}Xe nuclear spin polarization was 1×10^5 times greater than its thermal equilibrium polarization). The mixture was maintained at 3.5 bar and flowed at 0.1 SLPM. After polarization, the gas mixture was bubbled directly into a 10 mm NMR tube containing the MOF sample, and bubbling was stopped prior to each NMR scan.

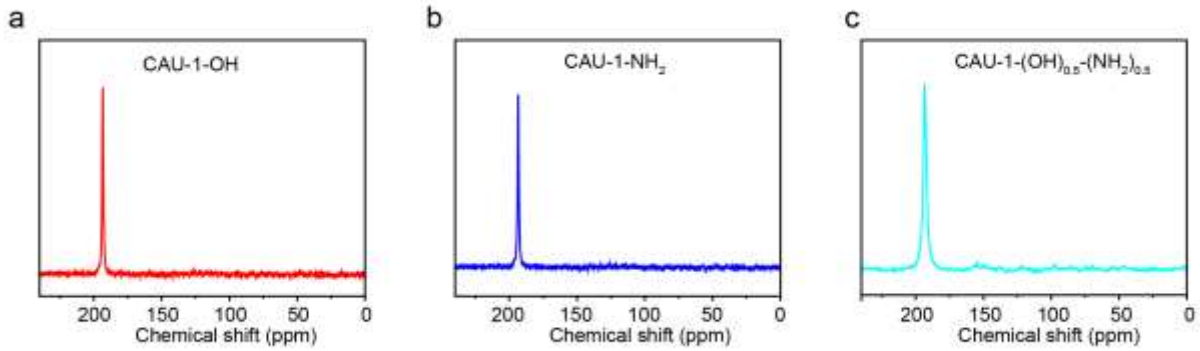

Figure S97. Hyperpolarized ^{129}Xe NMR spectra for CAU-1 (5 mg/mL) in aqueous solution.

13 Hyper-CEST MR procedures

13.1 Hyper-CEST NMR in solution

Hyperpolarized ^{129}Xe gas was produced by a home-built ^{129}Xe hyperpolarizer. A gas mixture of 10% N_2, 88% He, and 2% Xe (naturally abundant ^{129}Xe) was flowed through a home-made hyperpolarizer (hyperpolarized ^{129}Xe nuclear spin polarization was 1×10^5 times greater than its thermal equilibrium polarization). After the hyperpolarized gas mixture was directly bubbled into the NMR tube (10 mm NMR) for 20 s a 3-s delay time allowed the bubbles to collapse. A continuous-wave pulse (6.5 μT, 8 s) was then applied to saturate the Xe in the CAU-1 pores, and the ^{129}Xe NMR spectrum was acquired in a single scan. Spectra were processed using Lorentzian broadening (LB = 5 Hz).

13.1.1 Hyper-CEST regulated by particle size

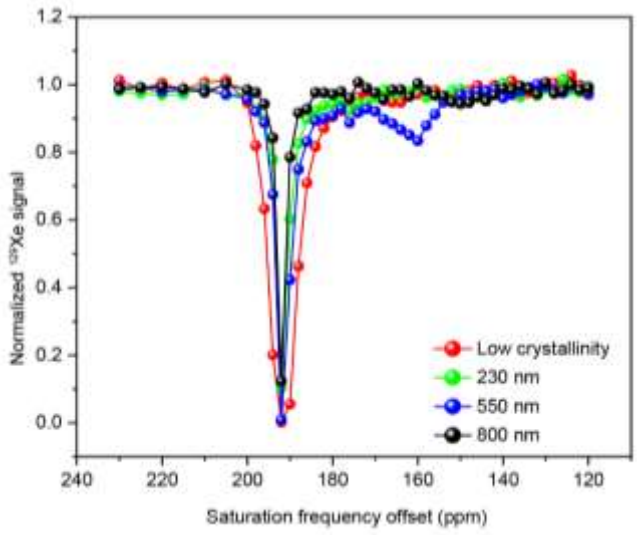

Figure S98. Hyper-CEST NMR spectra for different sizes of CAU-1-OH (100 μg/mL).

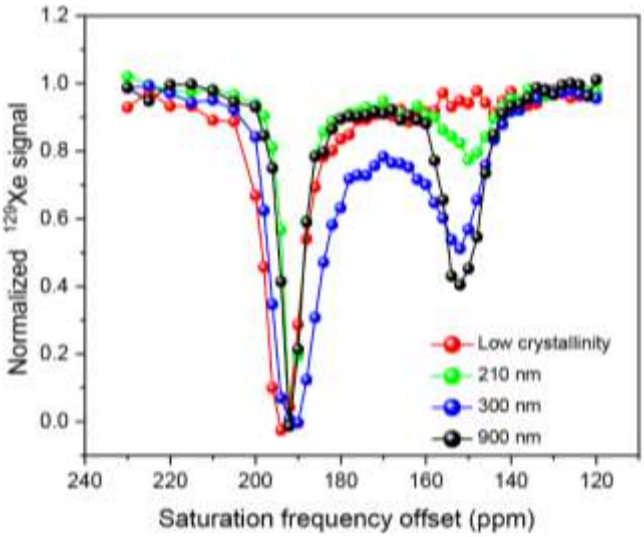

Figure S99. Hyper-CEST NMR spectra for different sizes of CAU-1-NH_2 (100 μg/mL).

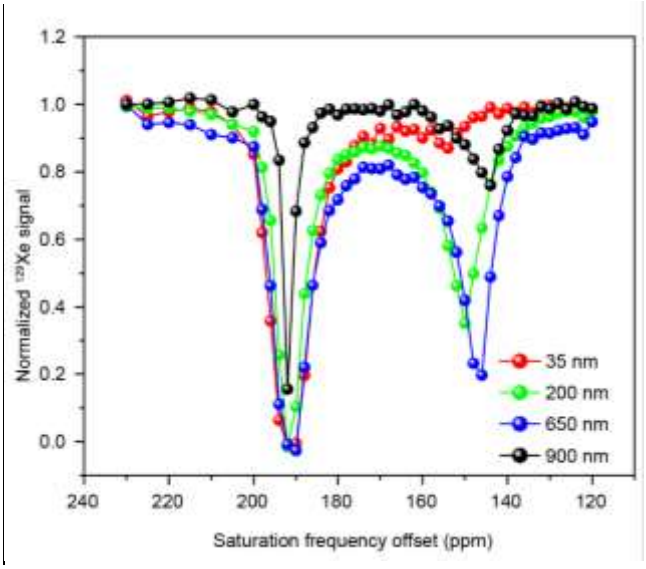

Figure S100. Hyper-CEST NMR spectra for different sizes of CAU-1-$(OH)_{0.5}$-$(NH_2)_{0.5}$ (100 μg/mL).

13.1.2 Hyper-CEST regulated by ligand ratio

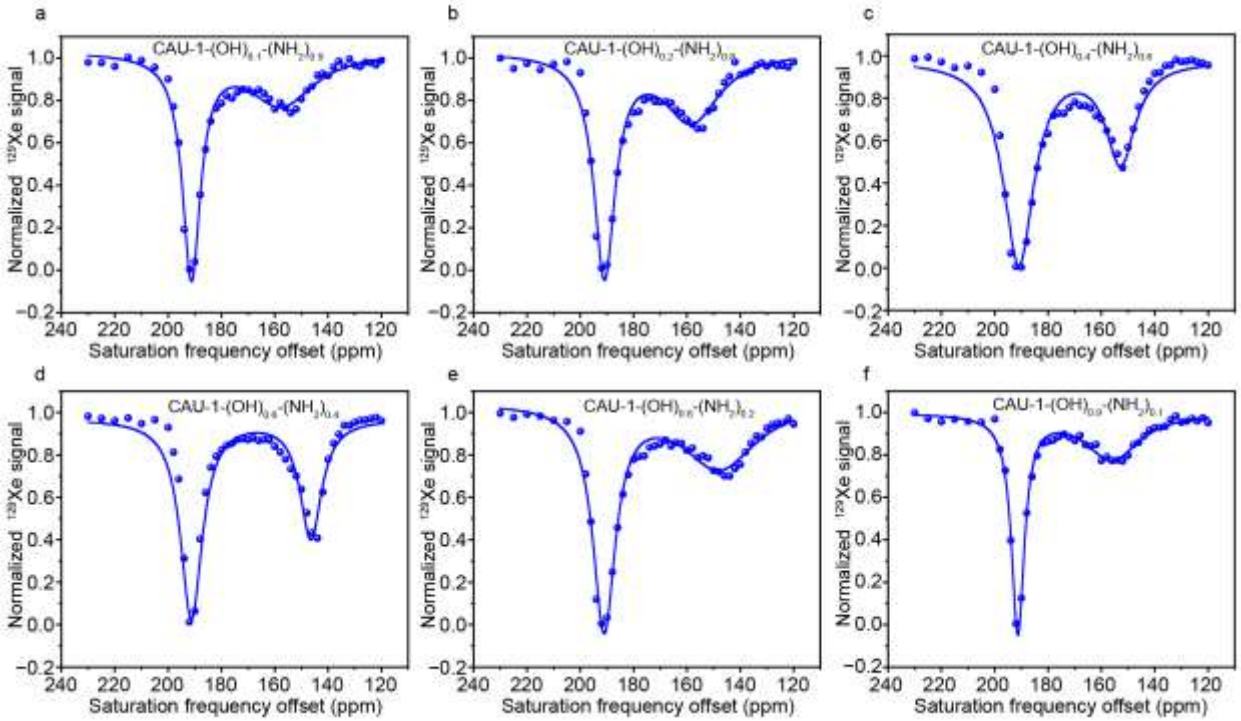

Figure S101. Hyper-CEST NMR spectra for different ligand ratios of CAU-1-$(OH)_x$-$(NH_2)_{1-x}$ (100 μg/mL).

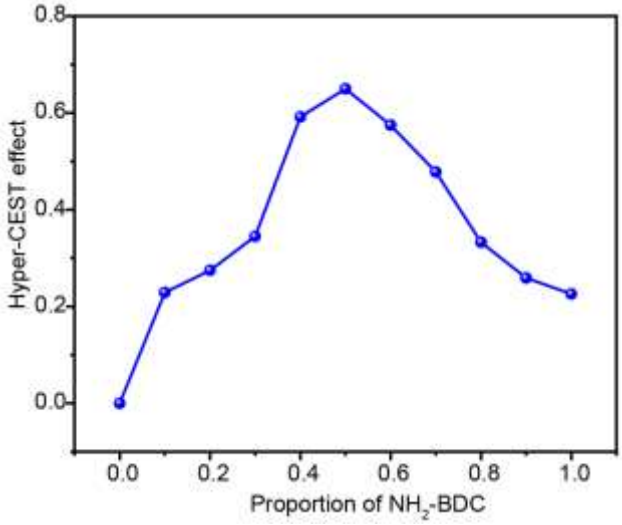

Figure S102. The relationship between Hyper-CEST effect and the proportion of amino group.

13.1.3 Hyper-CEST of CAU-1 immersed in water

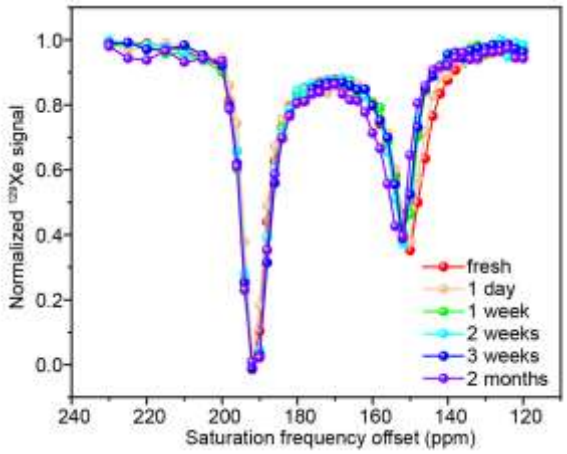

Figure S103. Hyper-CEST NMR spectra of CAU-1-$(OH)_{0.5}$-$(NH_2)_{0.5}$ immersed in water for different times.

13.1.4 Hyper-CEST of CAU-1-$(OMe)_{0.5}$-$(NH_2)_{0.5}$

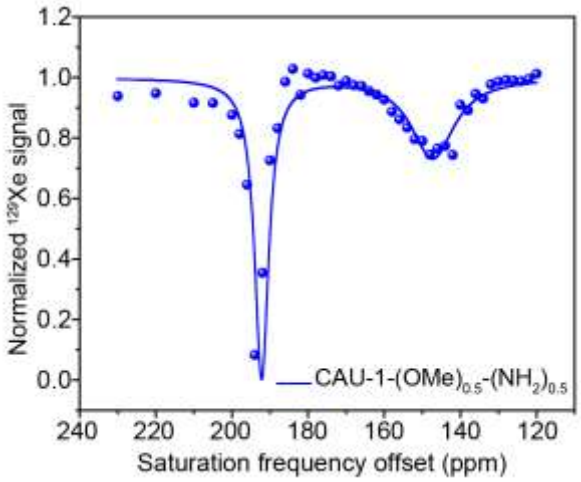

Figure S104. Hyper-CEST spectra of CAU-1-$(OMe)_{0.5}$-$(NH_2)_{0.5}$ (100 µg/mL).

13.2 Hyper-CEST MRI in solution

For the Hyper-CEST MRI experiment, 16 on-resonant and 16 off-resonant scans were acquired and averaged. The image was acquired using a RARE sequence (slice thickness = 30 mm, matrix size = 32 × 32, field of view = 30 × 30 mm^2, in-plane resolution = 0.9375 × 0.9375 mm^2, bandwidth = 5,400 Hz, echo time = 4.97 ms, repetition time= 82.3 ms, centric k-space encoding, no partial Fourier transform acceleration, RARE factor = 8). For each excitation, the Xe gas mixture was bubbled into the solution for a period of time (20 s), followed by a delay time (3 s) to allow the bubbles to collapse. After that, a saturation pulse was applied to saturate the Xe in the CAU-1 pores or off-resonance. Then, the image was acquired. The MR images were processed on MATLAB (R2014a; MathWorks). The image matrix 32 × 32 was interpolated into a 64 × 64 matrix. Hyper-CEST effect for on-resonant saturation was analyzed compared to off-resonant saturation for each pixel by the formula CEST effect = $(Intensity_{off}-Intensity_{on})/Intensity_{off}$ point by point.

13.2.1 Hyper-CEST MRI for different MOFs at the same concentrations

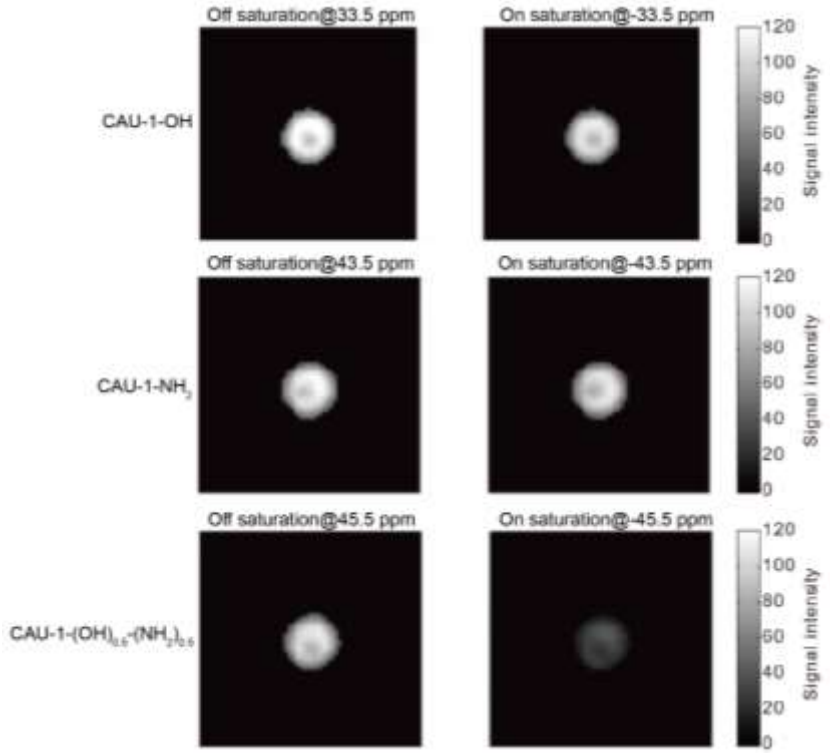

Figure S105. Hyper-CEST MR images of CAU-1-OH, CAU-1-NH_2, CAU-1-$(OH)_{0.5}$-$(NH_2)_{0.5}$ showing the average of 16 off-resonant and 16 on-resonant scans.

13.2.2 Concentration-dependent Hyper-CEST MRI

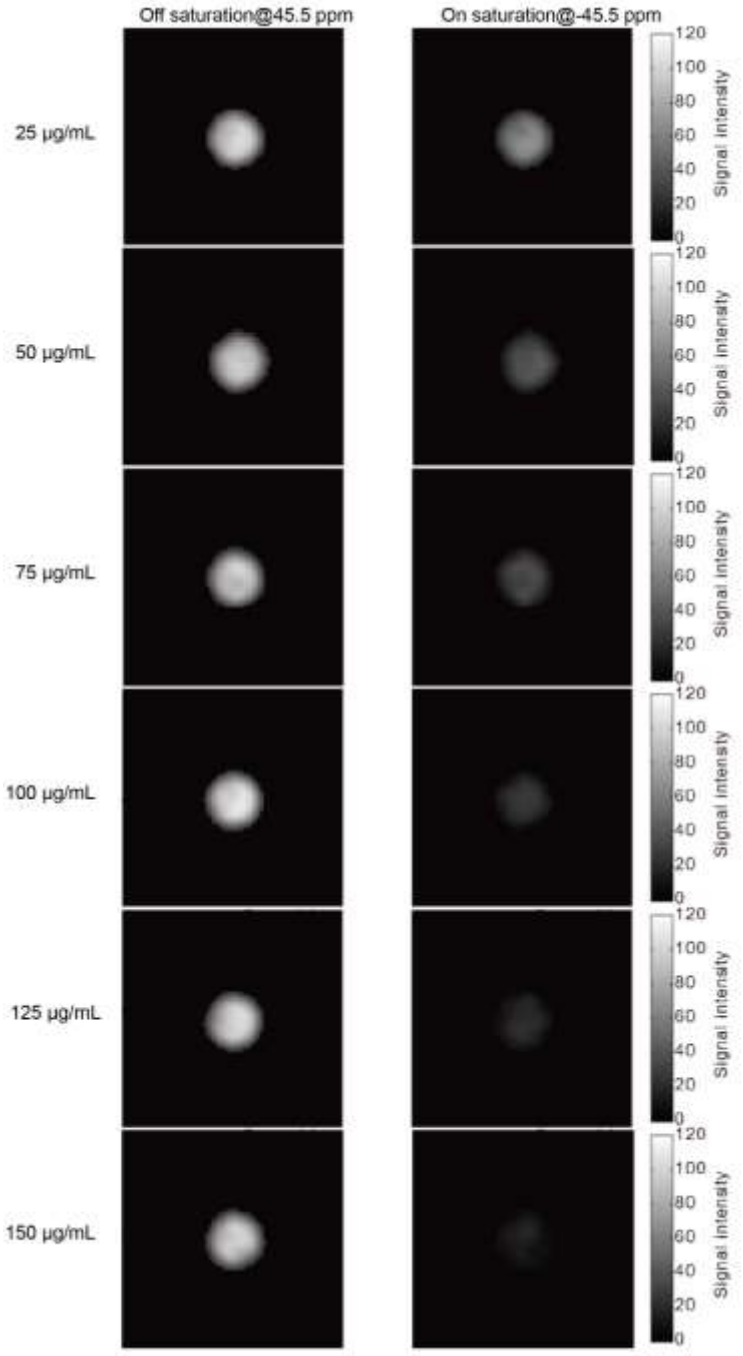

Figure S106. Hyper-CEST image of CAU-1-$(OH)_{0.5}$-$(NH_2)_{0.5}$ at different concentrations showing the average of 16 off-resonant (45.5 ppm, relative to dissolved Xe in solution at 0 ppm, left) and 16 on-resonant (-45.5 ppm, relative to dissolved Xe in solution at 0 ppm, right) scans.

13.3 Hyper-CEST of CAU-1 in A549 cells

Human lung cancer cells A549 were incubated in F12K supplemented with 10% fetal bovine serum and 1% penicillin−streptomycin at 37 °C in 5% CO_2 and 95% air environment. The cells were incubated with CAU-1-NH_2 or CAU-1-$(OH)_x$-$(NH_2)_{1-x}$ (75 μg/mL) and dispersed in culture medium for 2 h. The cells were washed three times with PBS at room temperature, followed by trypsinization and resuspension in culture medium. The cell concentration was kept at 7×10^6 cells/mL. Finally, the cells were transferred to a 10 mm NMR tube, and the ^{129}Xe NMR spectra were acquired by Hyper-CEST. For CEST experiment, a selective saturation pulse was swept across the chemical shift range of 120-170 ppm (cw-saturation for 8 s with a 6.5 μT field). The temperature was set to 298 K.

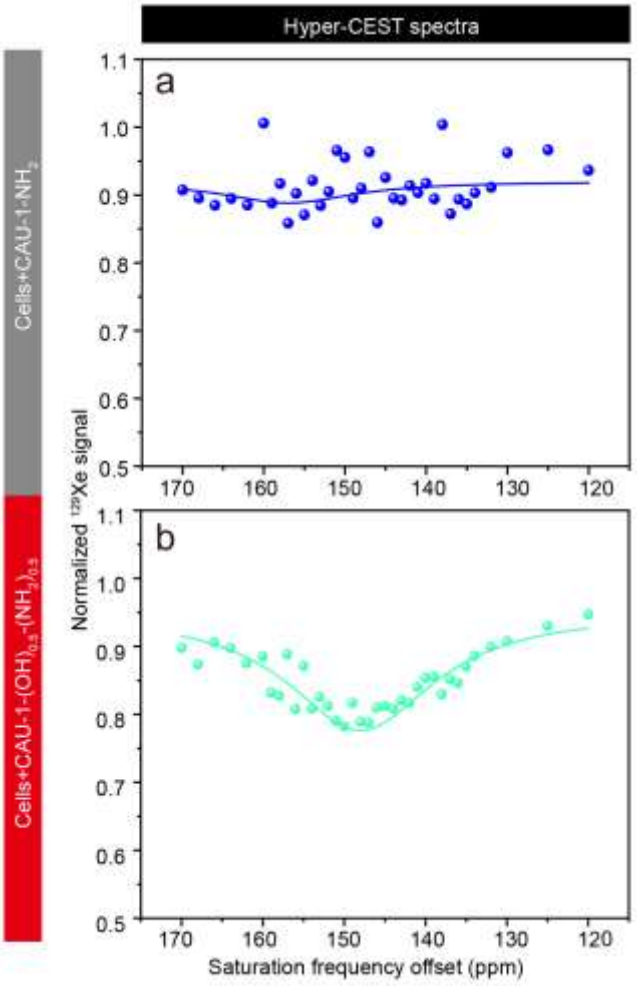

Figure S107. Hyper-CEST NMR spectra of (a) CAU-1-NH_2 and (b) CAU-1-$(OH)_{0.5}$-$(NH_2)_{0.5}$ in A549 cells.

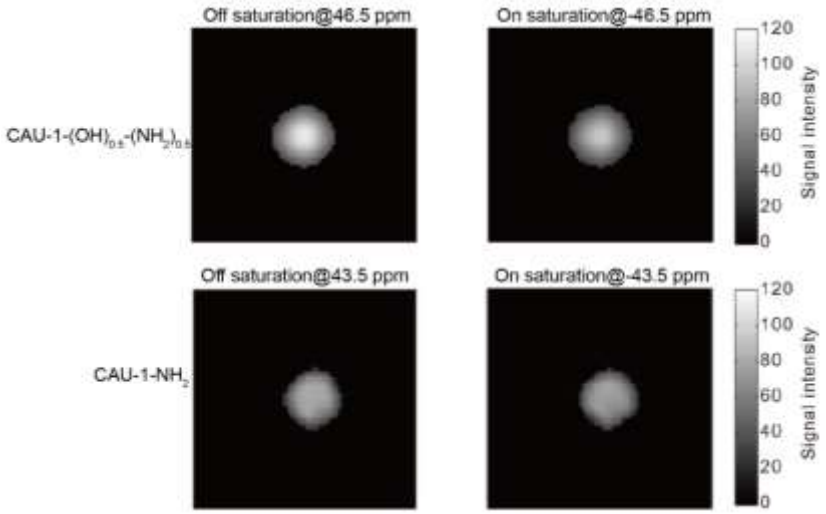

Figure S108. Hyper-CEST MR images of CAU-1-$(OH)_{0.5}$-$(NH_2)_{0.5}$ and CAU-1-NH_2 after incubation with live cells show the average of 16 off-resonant and 16 on-resonant scans.

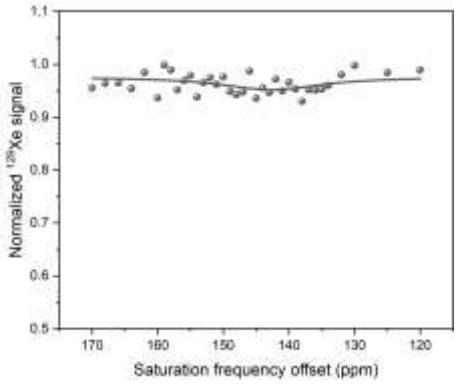

Figure S109. Hyper-CEST spectrum of A549 cells without MOF treatment.

14 Biological transmission electron microscopy

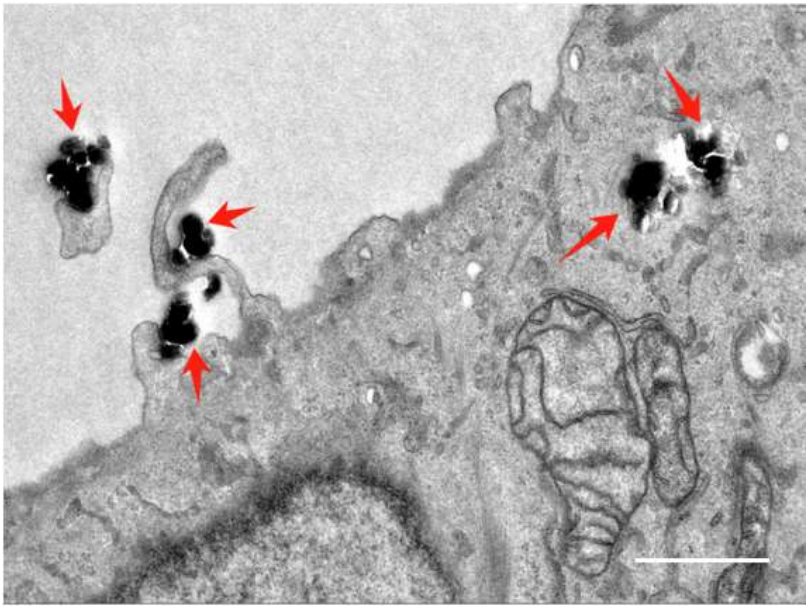

Figure S110. Biological transmission electron microscopy of CAU-1-OH after incubation with A549 cells. (Scale bar = 1000 nm)

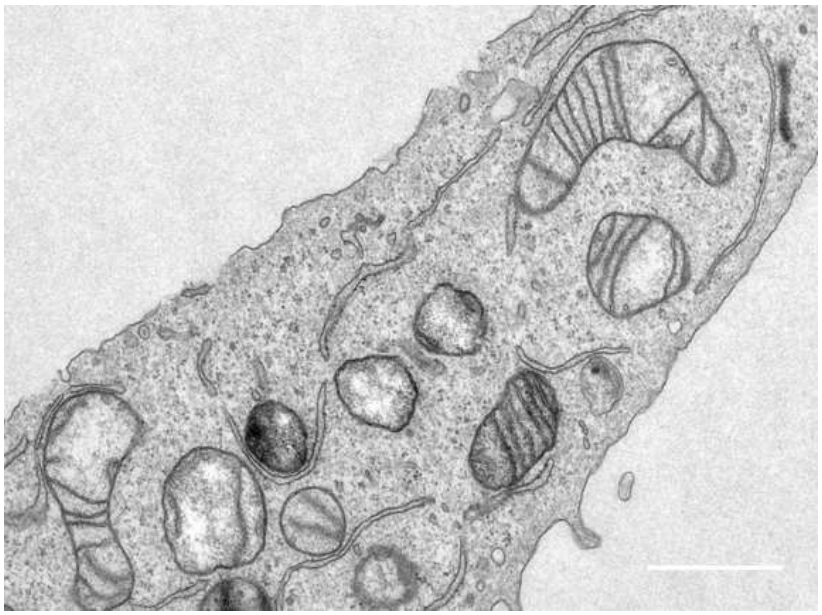

Figure S111. Biological transmission electron microscopy of normal A549 cells. (Scale bar = 1000 nm)

15 Biocompatibility Assays of CAU-1

15.1 CCK-8 Cell Viability Assay

Human bronchial epithelial BEAS-2B cells and human lung adenocarcinoma A549 cells were seeded separately into 96-well culture plates at the same cell density and cultured overnight to reach full adherence. Serial concentrations of different-sized CAU-1-$(OH)_{0.5}$-$(NH_2)_{0.5}$ suspensions ranging from 0 to 200 μg/mL were prepared in basal cell culture medium. The original culture medium was discarded, and each well was replenished with 100 μL of MOF suspension at the corresponding concentration. Cells were incubated with MOF samples for 6 h at 37 °C under a humidified atmosphere containing 5% CO_2. After 6 h incubation, the MOF-containing medium in each well was completely aspirated, and then 110 μL basal cell culture medium premixed with 10 μL CCK-8 working solution was added to each well. The plates were incubated for an additional approximately 2 h to facilitate color development. The absorbance of each well at 450 nm was recorded using a microplate reader. Cell viability was calculated via the following formula:

$$\text{Cell viability (\%)} = \frac{OD_{sample} - OD_{blank}}{OD_{control} - OD_{blank}} \times 100\%$$

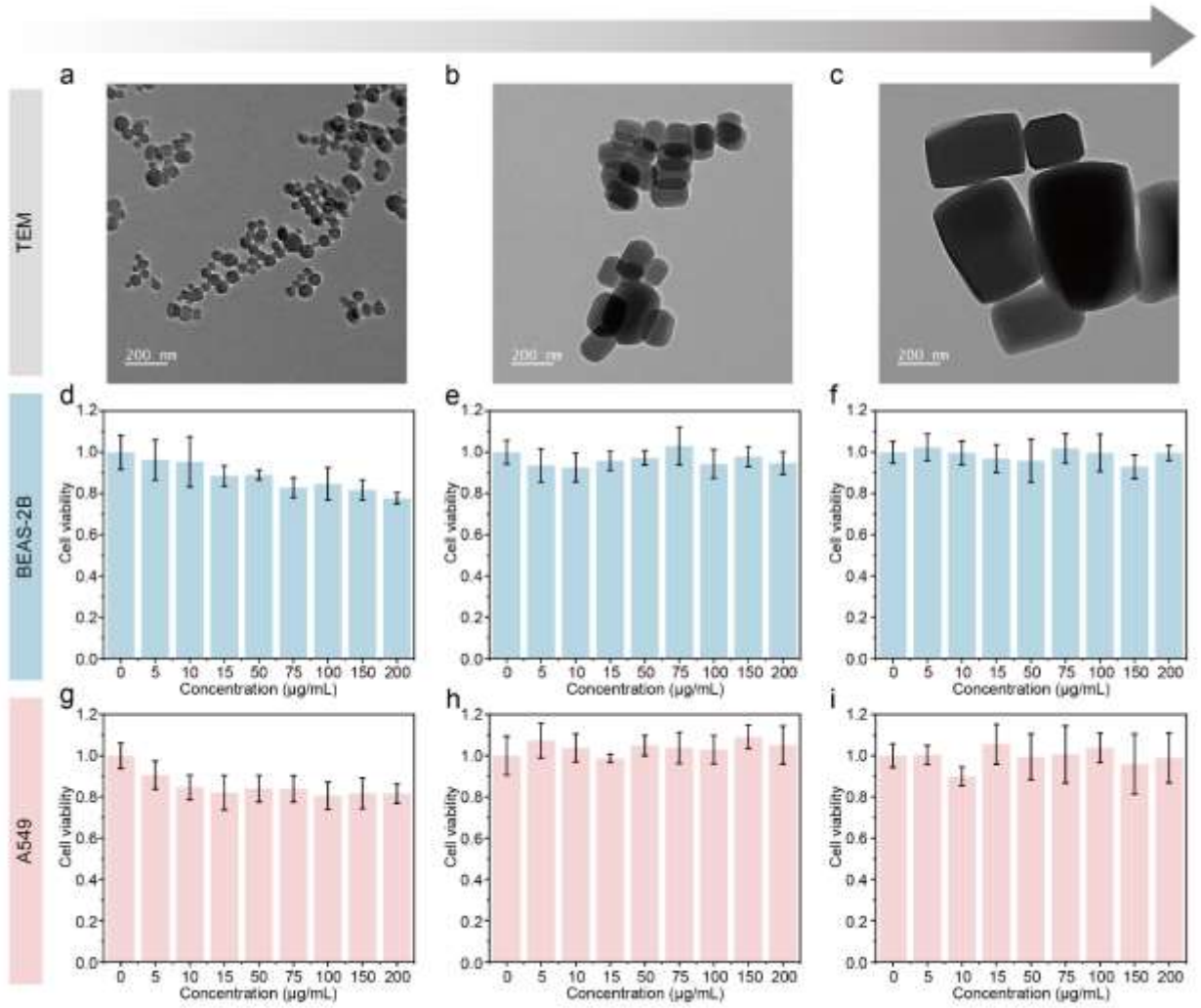

Figure S112. (a–c) TEM images of CAU-1-$(OH)_{0.5}$-$(NH_2)_{0.5}$ with different particle sizes. (d–f) Cell viability of BEAS-2B cells after incubation with CAU-1-$(OH)_{0.5}$-$(NH_2)_{0.5}$ of different particle sizes at various concentrations for 6 h, as determined by the CCK-8 assay. (g–i) Cell viability of A549 cells after incubation with CAU-1-$(OH)_{0.5}$-$(NH_2)_{0.5}$ of different particle sizes at various concentrations for 6 h, as determined by the CCK-8 assay. Data are presented as mean ± SD (n = 6).

15.2 Hemolysis Assay of Nanomaterials

Whole blood was harvested from healthy BALB/c mice via retro-orbital bleeding, and immediately transferred into anticoagulant tubes preloaded with EDTA or sodium citrate. After gentle mixing, the blood sample was centrifuged at 3000 rpm for 15 min to collect red blood cells (RBCs) for subsequent hemolysis quantification of nanoparticles.

Gradient concentrations of nanomaterial suspensions (25–500 μg/mL) were prepared in 0.9% NaCl solution. For each group, 1 mL nanomaterial suspension, 1 mL ddH_2O (positive control), and 1 mL 0.9% NaCl solution (negative control) were individually mixed with 20 μL purified RBC suspensions. All mixtures were incubated at 37 °C for 4 h, followed by centrifugation at 3000 rpm for 15 min. The tubes were aligned on a horizontal surface, and digital photographs were captured to record macroscopic hemolysis phenomena.

Subsequently, the supernatant of each sample was carefully aspirated using a pipette. The absorbance at 542 nm was measured with a microplate reader. All groups were conducted in biological triplicate, and standard deviation (SD) was calculated for statistical analysis.

The hemolysis percentage was calculated according to the following formula:

$$\text{Hemolysis rate (\%)} = \frac{OD_{sample} - OD_{NaCl}}{OD_{ddH_2O} - OD_{NaCl}} \times 100\%$$

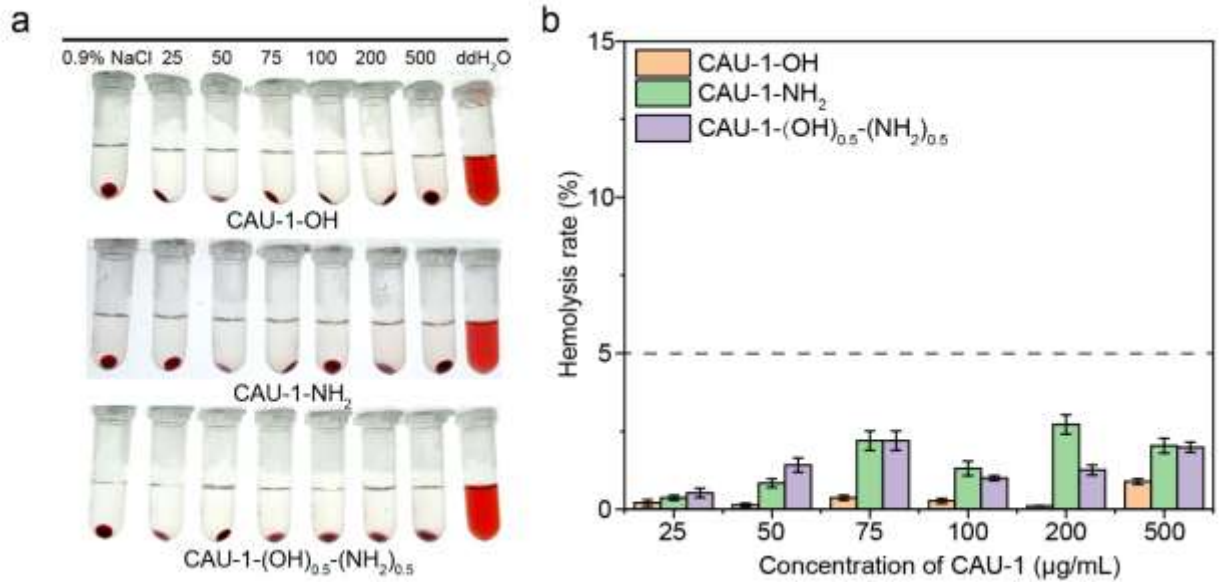

Figure S113. (a) Representative photographs of the hemolysis assay for CAU-1-OH, CAU-1-NH_2, and CAU-1-$(OH)_{0.5}$-$(NH_2)_{0.5}$ at different concentrations. Physiological saline (0.9% NaCl) and deionized water were used as the negative and positive controls, respectively. (b) Quantitative hemolysis ratios of CAU-1-OH, CAU-1-NH_2, and CAU-1-$(OH)_{0.5}$-$(NH_2)_{0.5}$ at different concentrations. Data are presented as mean ± SD (n = 3).

16 Data comparison tables

Table S1. Summary of BET data for CAU-1-OH at different sizes

Size of CAU-1-OH	BET Surface Area (m^2/g)	Total pore volume (cm^3/g)	t-Plot micropore volume (cm^3/g)	Pore width (Å)
Low crystallinity	1003	0.39	0.35	8.014
230	1174	0.51	0.45	8.476
550	756	0.33	0.29	8.358
800	1003	0.32	0.30	8.014

Table S2. Summary of BET data for CAU-1-NH_2 at different sizes

Size of CAU-1-NH_2	BET Surface Area (m^2/g)	Total pore volume (cm^3/g)	t-Plot micropore volume (cm^3/g)	Pore width (Å)
Low crystallinity	1179	0.67	0.44	8.728
210	1308	0.57	0.5	8.551
300	1194	0.52	0.45	8.361
900	1383	0.49	0.40	8.042

Table S3. Summary of BET data for CAU-1-$(OH)_{0.5}$-$(NH_2)_{0.5}$ at different sizes

Size of CAU-1-$(OH)_{0.5}$-$(NH_2)_{0.5}$	BET Surface Area (m^2/g)	Total pore volume (cm^3/g)	t-Plot micropore volume (cm^3/g)	Pore width (Å)
35	1256	0.66	0.47	8.728
200	1239	0.54	0.43	8.054
650	1199	0.50	0.45	8.538
900	1569	0.49	0.44	8.014

Table S4. Summary of BET data for different ligand ratios of CAU-1-$(OH)_x$-$(NH_2)_{1-x}$

Samples	BET Surface Area (m^2/g)	Total pore volume (cm^3/g)	t-Plot micropore volume (cm^3/g)	Pore width (Å)
CAU-1-NH_2	1308	0.57	0.5	8.551
CAU-1-$(OH)_{0.1}$-$(NH_2)_{0.9}$	1350	0.64	0.46	8.069
CAU-1-$(OH)_{0.2}$-$(NH_2)_{0.8}$	1397	0.64	0.48	8.098
CAU-1-$(OH)_{0.3}$-$(NH_2)_{0.7}$	1442	0.67	0.50	8.127
CAU-1-$(OH)_{0.4}$-$(NH_2)_{0.6}$	1502	0.68	0.52	8.132
CAU-1-$(OH)_{0.5}$-$(NH_2)_{0.5}$	1239	0.54	0.43	8.054
CAU-1-$(OH)_{0.6}$-$(NH_2)_{0.4}$	1541	0.66	0.54	8.174
CAU-1-$(OH)_{0.7}$-$(NH_2)_{0.3}$	1541	0.68	0.54	8.15
CAU-1-$(OH)_{0.8}$-$(NH_2)_{0.2}$	1576	0.68	0.55	8.141
CAU-1-$(OH)_{0.9}$-$(NH_2)_{0.1}$	1630	0.71	0.57	8.181
CAU-1-OH	1174	0.51	0.45	8.476

References

[1] Kresse, G.; Joubert, D. From ultrasoft pseudopotentials to the projector augmented - wave method. *Phys. Rev. B.* **1999**, 59, 1758-1775.

[2] Perdew, J. P.; Burke, K.; Ernzerhof, M. Generalized gradient approximation made simple. *Phys. Rev. Lett.* **1996**, 77, 3865-3868.

[3] Grimme, S.; Antony, J.; Ehrlich, S.; Krieg, H. A consistent and accurate ab initio parametrization of density functional dispersion correction (DFT-D) for the 94 elements H-Pu. *J. Chem. Phys.* **2010**, 132, 154104.